IEEE Access
Multidisciplinary | Rapid Review | Open Access Journal

Received August 24, 2021, accepted October 12, 2021, date of publication October 15, 2021, date of current version October 25, 2021.

Digital Object Identifier 10.1109/ACCESS.2021.3120380

Harmonic-Separation-Based Direct Extraction and Compensation of Inverter Nonlinearity for State Observation Control of PMSM

SHICHAO ZHOU[1], KAN LIU[1], (Senior Member, IEEE), WEI HU[1], YONGDAN CHEN[2], DINGHUA ZHANG[3], QING HUANG[3], QIAOLING TONG[4], (Member, IEEE), AND QIAO ZHANG[5], (Member, IEEE)

[1]College of Mechanical and Vehicle Engineering, Hunan University, Changsha 410082, China
[2]China North Vehicle Research Institute, Beijing 100071, China
[3]China Railway Rolling Stock Corporation, Zhuzhou 412000, China
[4]School of Optical and Electronic Information, Huazhong University of Science and Technology, Wuhan 430074, China
[5]School of Automation, Wuhan University of Technology, Wuhan 430070, China

Corresponding author: Kan Liu (lkan@hnu.edu.cn)

This work was supported by the National Natural Science Foundation of China under Grant 51877075.

ABSTRACT Nonideal switching characteristics of voltage source inverter (VSI) will result in distortions in both phase currents and reference voltages of a permanent magnet synchronous machine (PMSM) drive system, which will also consequently introduce ripples into the output speed and shaft torque, and result in a performance deterioration in the state observation control. To solve this issue, a method of directly extracting and compensating the nonlinear voltage disturbance due to VSI nonlinearity employed in PMSM drives is proposed in this paper. Firstly, the distorted voltage due to VSI nonlinearity is directly extracted via a harmonic separation scheme, which can be easily compensated by a proportional integral controller afterwards. Since both 6th harmonic and DC terms of dq-axis distorted voltages due to VSI nonlinearity are well compensated, the proposed method shows sufficiently good performance under both $i_d = 0$ and maximum torque per ampere controls ($i_d < 0$), as verified on two prototype PMSMs being salient pole and non-salient pole, respectively, both developed for a low-speed rotary actuator. In addition, the application of proposed method to state observation controls such as the model-based sensorless control and the deadbeat predictive current control, is finally investigated. Test results manifest that the proposed method can effectively improve the accuracy of observed rotor position/speed, and the ability of current tracking.

INDEX TERMS Harmonic separation, permanent magnet synchronous machine (PMSM), state observation control, voltage disturbance, voltage source inverter (VSI) nonlinearity.

NOMENCLATURE

V_{dead}	Distorted voltage term due to voltage source inverter nonlinearity (V).
T_s, T_{dead}	Switching period and dead time (μs).
T_{on}, T_{off}	Turn-on/turn-off delay of switching tubes (μs).
V_{dc}	DC link voltage (V).
V_{sat}, V_d	Forward voltage drops of switching tubes and freewheeling diodes (V).
L_d, L_q	dq-axis inductances (H).
R_s	Stator winding resistance (Ω).
ψ_m	Rotor permanent magnet flux linkage (Wb).
ω, ω_e	Mechanical and electrical speed (rad/s).
θ, θ_e	Rotor electrical position, and $\theta = \theta_e + \pi/2$ (rad).
$\wedge$	Denoting the estimated value.

The associate editor coordinating the review of this manuscript and approving it for publication was Jinquan Xu.

I. INTRODUCTION

The conventional three-phase half-bridge inverter and space vector pulse width modulation (SVPWM) techniques have been extensively employed in drive control of permanent magnet synchronous machines (PMSMs), which usually work on the assumption that the switching characteristics of power devices are ideal. However, in reality, nonlinearities of voltage source inverters (VSIs), such as dead time,

switch-on/switch-off delay, and forward voltage drops due to on-state insulated gate bipolar translators (IGBTs) and freewheeling diodes, would result in a mismatch between reference voltages and real ones of PMSMs, and ultimately lead to non-negligible 6th order harmonic in the synchronous reference frame [1]–[3]. The voltage distortion due to 6th order harmonic would eventually generate disturbances in three-phase currents, output torque and rotor speed, especially in low-speed applications.

Furthermore, stator observation control such as sensorless control and deadbeat predictive current control (DPCC) are now widely used in the high-performance drive control of PMSMs. In reality, the VSI nonlinearity can cause 5th and 7th harmonics of $\alpha\beta$-axis estimated back electromotive force (EMF) in the model-based sensorless technique [4], which degrades the accuracy of rotor position/speed estimation. And on account of the voltage distortion resulted from VSI nonlinearity, the tracking performance of stator current gets worse in the DPCC. Overall, accurate machine voltages and low-harmonic stator current are usually essential for the model-based sensorless control and DPCC [5], which need a precise compensation on the VSI nonlinearity. Thus, the compensation of VSI nonlinearity has been extensively studied recently in both academia and industry, whose mainstream methods can be classified into two main types being reviewed below.

The first type can be regarded as a pulse-based correction scheme, which adjusts gating signals of power devices to compensate those nonlinear effects and needs accurate detection of current polarities [6]–[14]. A simple solution is to directly determine polarities of three-phase currents according to current sensors [6]–[12] or terminal voltages [13], whose accuracy depends on the analog-to-digital converter (ADC). And a circuit for the detection of current polarities is proposed in [14], which can significantly improve the accuracy of detection [14]. However, it would result in higher cost and increase the complexity of hardware system. Besides, it would be simpler if only the influence of dead time is taken into account [6]–[9] whereas the accuracy of compensation is still unsatisfactory in low DC link voltage applications, in which on-state voltage drops of power devices and turn-on/off delay play quite important roles in three-phase voltages [10]–[13]. Although the voltage drop is taken into consideration in [11], it is regarded as a constant and the accuracy of compensation cannot be guaranteed under changeable phase current conditions. Furthermore, the curve between the conduction voltage drops of power devices and phase currents can be measured from experimental tests [15], whose precision really depends on the stator resistance of the measurement model.

The second type, which takes into account the estimation and compensation of VSI nonlinearities including on-state voltage drops of power devices, dead time, switch-on/off delay etc. and does not require offline tests, has now become the mainstream solution in recent studies [16]–[30]. This solution is based on the average value theory in which the volt-second error in a switching cycle is compensated to the reference voltage, then the reference voltage acts on the SVPWM to generate the drive signal of IGBTs. In this solution, a disturbance voltage term is usually defined for representing the voltage distortion due to VSI nonlinearities, and will be estimated and compensated by way of harmonic analysis [16]–[23] or disturbance voltage observer [24]–[30].

The former one, being based on harmonic analysis, can extract the disturbance voltage term from reference voltages or measured currents, which can be employed for the online compensation of VSI nonlinearity afterwards. For example, it is reported in [16]–[23] that the VSI nonlinearity can be approximately compensated via the minimization of harmonics. Specifically, the disturbance voltage term can be identified by waveform analysis [17], self-commissioning algorithm [18], iterative learning control (ILC) [19], total least square algorithm [20], current injection [21], neural network [22], [23] and so on. The strategy in [17] is insensitive to the variation of machine parameters, whereas it only works well at steady state, and the estimation process of disturbance voltage is also relatively slow at low-speed region due to the calculation of average slope. In [18], the proposed algorithm enhances the accuracy of flux identification, and has a good application in induction motor drives. According to eliminating harmonics in the estimated d-axis back EMF, the method in [19] achieves a better performance in sensorless control. Note that the update law gain of ILC needs to be carefully selected, otherwise the algorithm cannot converge. Similarly, it is proposed in [20] to estimate the disturbance voltage by eliminating the harmonics of estimated back EMF. In [21], current injection is used to estimate VSI nonlinearity, but its application is quite limited due to the ripple generated during injection. As detained in [22] and [23], adjusting the weight factor of neural network can estimate VSI nonlinearity online, but the design of algorithms is relatively complex. In addition, the PMSM model can be simplified by using $i_d = 0$ to be less parameter-dependent and achieve the nonlinearity compensation [16], [22]. However, it would not be effective for $i_d < 0$ control, for example, the maximum torque per ampere (MTPA) control of an interior permanent magnet synchronous machine (IPMSM). It is noted that the disturbance voltage varies with the angle between current vector and q-axis [26], that is, the disturbance voltage is related to the control mode. Research on the compensation of VSI nonlinearity under MTPA control is presented in [31], which utilizes the resistance of inverter and machine to calculate the voltage error.

The observer based method usually has good performance in the identification of the disturbance voltage term, whereas it inherently relies on the accuracy of electrical machine parameters [24]–[30]. In this scheme, the observed disturbance voltage term is compensated online, and the observation error due to parameter variation will act directly on the control system. In short, the observer based method is usually quite sensitive to machine parameters, and its accuracy would deteriorate in applications with uncertain or

TABLE 1. Distorted voltages caused by VSI nonlinearity under different current polarities.

Case	θ_e	$sign(i_{a,b,c})$			$V_{dead}Dd$	$V_{dead}Dq$
		i_a	i_b	i_c		
1	-π/6-λ~π/6-λ	1	-1	-1	$4V_{dead}\sin(\theta_e)$	$4V_{dead}\cos(\theta_e)$
2	π/6-λ~π/2-λ	1	1	-1	$4V_{dead}\sin(\theta_e-\pi/3)$	$4V_{dead}\cos(\theta_e-\pi/3)$
3	π/2-λ~5π/6-λ	-1	1	-1	$4V_{dead}\sin(\theta_e-2\pi/3)$	$4V_{dead}\cos(\theta_e-2\pi/3)$
4	5π/6-λ~7π/6-λ	-1	1	1	$4V_{dead}\sin(\theta_e-\pi)$	$4V_{dead}\cos(\theta_e-\pi)$
5	7π/6-λ~3π/2-λ	-1	-1	1	$4V_{dead}\sin(\theta_e-4\pi/3)$	$4V_{dead}\cos(\theta_e-4\pi/3)$
6	3π/2-λ~11π/6-λ	1	-1	1	$4V_{dead}\sin(\theta_e-5\pi/3)$	$4V_{dead}\cos(\theta_e-5\pi/3)$

changeable machine parameters. In particular, it is proposed in [26] to indirectly observe an intermediate parameter to calculate the voltage distortion, which avoids the observation delay caused by filtering. In fact, the intermediate parameter is the distorted voltage term V_{dead} in this paper, whereas the proposed method in this paper does not require any machine parameters. Furthermore, a simplified model of PMSM is needed to establish a disturbance observer [25], [29], for example, $i_d = 0$.

As analyzed hereinbefore, the pulse-based correction scheme usually only considers the nonlinearity due to switching time delay and dead time, or requires offline tests in low DC link voltage applications. As for the scheme based on estimation and compensation of VSI nonlinearities, the harmonic analysis based method usually has relatively complex design of algorithms or can only work well at steady state and $i_d = 0$ control, while the observer based method is quite parameter-dependent. In order to achieve simplicity, multi-mode controls and parameter-independence in the compensation of VSI nonlinearities, a method of directly extracting and compensating the nonlinear voltage disturbance is proposed in this paper. It extracts the disturbance voltage term according to a harmonic separation scheme, which is parameter-independent and needs quite few calculations. Afterwards, the determined distorted voltage term is eventually online compensated by a close-loop proportional integral (PI) control. Since both 6th harmonic and DC terms in dq-axis distorted voltages are considered in the extraction model, it can be employed for both $i_d = 0$ and $i_d \neq 0$ controls. The effectiveness of proposed method is finally evaluated on a non-salient pole surface-mounted PMSM (SPMSM) and a salient pole IPMSM, respectively, which shows quite good performance under both $i_d = 0$ and MTPA controls ($i_d \neq 0$). Besides, the application of proposed method to state observation control is also verified. Experimental results show that the proposed method can significantly improve the performance of state observation controls such as the sensorless control and the DPCC. The whole paper is organized as follows: Section II is about the theory fundamentals of extraction of disturbance voltage due to VSI nonlinearity; Section III introduces the design of a feedback PI control to suppress the VSI nonlinearity; Section IV shows the experimental verifications and analyses; Section V details the application of proposed method to state observation controls.

II. MODELING OF PMSM DRIVE SYSTEM AND EXTRACTION OF DISTORTED VOLTAGE DUE TO VSI NONLINEARITY

A. MODELING OF PMSM DRIVE SYSTEM

Neglecting the influence of cross-coupling effect and the measurement error of DC link voltage, the dq-axis voltage equations of PMSM considering VSI nonlinearity can be expressed as follows: [25]–[29]

$$\begin{cases} u_d^* = R_s i_d + L_d \dfrac{di_d}{dt} - L_q i_q \omega_e + V_{dead} Dd \\ u_q^* = R_s i_q + L_q \dfrac{di_q}{dt} + L_d i_d \omega_e + \omega_e \psi_m + V_{dead} Dq \end{cases} \tag{1}$$

where u_d^* and u_q^* are dq-axis reference voltages, i_d and i_q are dq-axis currents, $V_{dead}Dd$ and $V_{dead}Dq$ are dq-axis distorted voltage terms due to VSI nonlinearity. V_{dead} can be considered as a constant at steady state, and it can be written as [25], [27]

$$V_{dead} = \frac{T_{dead} + T_{on} - T_{off}}{3T_s}(V_{dc} - V_{sat} + V_d) + \frac{V_{sat} + V_d}{6}. \tag{2}$$

In addition, Dd and Dq are functions of electrical angular position and current polarities, and can be expressed below:

$$\begin{bmatrix} Dd \\ Dq \end{bmatrix} = 2 \begin{bmatrix} \cos(\theta)\cos\left(\theta - \frac{2\pi}{3}\right)\cos\left(\theta + \frac{2\pi}{3}\right) \\ -\sin(\theta) - \sin\left(\theta - \frac{2\pi}{3}\right)\sin\left(\theta - \frac{2\pi}{3}\right) \end{bmatrix} \times \begin{bmatrix} sign(i_a) \\ sign(i_b) \\ sign(i_c) \end{bmatrix} \tag{3}$$

$$sign\left(i_{a,b,c}\right) = \begin{cases} 1, & i_{a,b,c} \geq 0 \\ -1, & i_{a,b,c} < 0 \end{cases} \tag{4}$$

where $i_{a,b,c}$ represents one of three-phase currents.

As shown in Table 1, Dd and Dq will vary under different current polarities and electrical angular position [28] while λ is the current angle between current vector and q-axis, as indicated in Appendix A. The current angle λ determines the average values of $V_{dead}Dd$ and $V_{dead}Dq$ in theory. For example, in the first case of Table 1, $Dd = 4\sin(\theta_e)$ and $Dq = 4\cos(\theta_e)$ while in the second case, $Dd = 4\sin(\theta_e - \pi/3)$ and $Dq = 4\cos(\theta_e - \pi/3)$, etc. Thus, Dd and Dq can also be re-written as follows:

$$\begin{bmatrix} Dd \\ Dq \end{bmatrix} = 4 \begin{bmatrix} \sin(\theta_e + \alpha) \\ \cos(\theta_e + \alpha) \end{bmatrix} \tag{5}$$

where α could be 0, -π/3, -2π/3, -π, -4π/3, or -5π/3, as shown in Table 1. As a result, the frequency of distorted voltage due to VSI nonlinearity will be 6 times of fundamental frequency in theory, which can also be validated by experiments as shown in Fig. 1. It can be seen in Fig. 1(a) that during

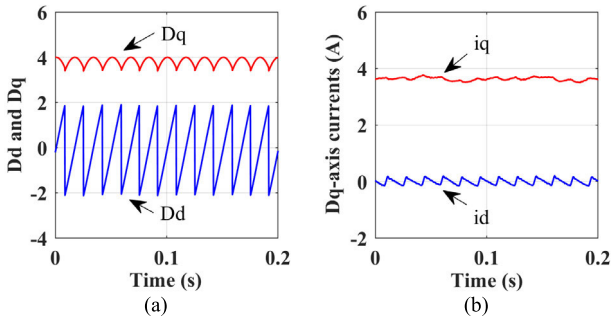

FIGURE 1. Measured waveforms from experiments on SPMSM under $i_d = 0$ control ($\lambda = 0{,}150$r/min and 2.0N·m). (a) *Dd* and *Dq*. (b) *dq*-axis currents.

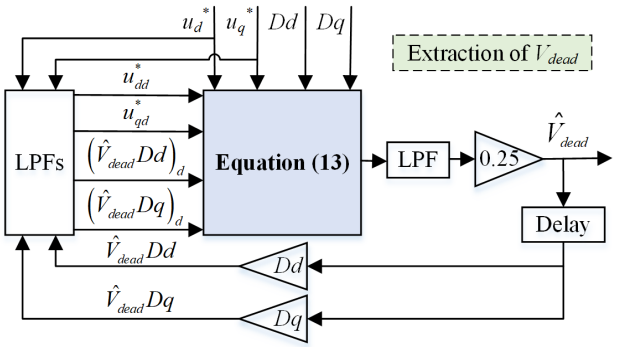

FIGURE 2. Block diagram of extraction of V_{dead} via proposed harmonic separation.

the test, calculated *Dd* and *Dq* are oscillating at 6 times of fundamental frequency (10Hz). Consequently, resulting 6th harmonic will be introduced into *dq*-axis currents, as shown in Fig. 1(b), and generate ripples in both the output torque and speed, and eventually result in deterioration of control performance.

B. EXTRACTION OF DISTORTED VOLTAGE DUE TO VSI NONLINEARITY

According to the theory of Fourier series expansion, a periodic signal can be expressed as the synthesis of DC and harmonic components. Thus, the *dq*-axis reference voltages of a PMSM drive system can be expressed as follows:

$$\begin{cases} u_d^* = u_{dd}^* + u_{dh}^* \\ u_q^* = u_{qd}^* + u_{qh}^* \end{cases} \tag{6}$$

where u_{dd}^* and u_{qd}^* are DC components of *dq*-axis reference voltages; u_{dh}^* and u_{qh}^* are harmonic components.

Similarly, the *dq*-axis distorted voltages caused by VSI nonlinearity can be represented as follows:

$$\begin{cases} V_{dead}Dd = (V_{dead}Dd)_d + (V_{dead}Dd)_h \\ V_{dead}Dq = (V_{dead}Dq)_d + (V_{dead}Dq)_h \end{cases} \tag{7}$$

where $(V_{dead}Dd)_d$ and $(V_{dead}Dq)_d$ are DC components of the distorted voltages; $(V_{dead}Dd)_h$ and $(V_{dead}Dq)_h$ are harmonic components. u_{dd}^*, u_{qd}^*, $(V_{dead}Dd)_d$ and $(V_{dead}Dq)_d$ can be extracted by low-pass filters (LPFs), as shown in Fig. 2.

In order to extract the distorted voltage term V_{dead} generated by VSI nonlinearity, a harmonic separation scheme is proposed in this paper and introduced below:

Firstly, u_{dh}^* and u_{qh}^* in (6) can be re-written as follows:

$$\begin{cases} u_{dh}^* = (V_{dead}Dd)_h + u_{dh} \\ u_{qh}^* = (V_{dead}Dq)_h + u_{qh} \end{cases} \tag{8}$$

where u_{dh} and u_{qh} are *dq*-axis harmonic components except VSI nonlinearity, which are mainly related to back EMF harmonics, cogging torque, etc. It should be noted that for those low voltage/low speed PMSMs, the harmonics generated by the VSI nonlinearity are usually dominant compared with other harmonic sources.

Through (6)-(8), *dq*-axis reference voltages can be eventually re-written as follows:

$$\begin{cases} u_d^* = u_{dd}^* + V_{dead}Dd - (V_{dead}Dd)_d + u_{dh} \\ u_q^* = u_{qd}^* + V_{dead}Dq - (V_{dead}Dq)_d + u_{qh}. \end{cases} \tag{9}$$

Substituting (5) into (9) yields:

$$u_d^* - u_{dd}^* + (V_{dead}Dd)_d = 4V_{dead}\sin(\theta_e + \alpha) + u_{dh} \tag{10a}$$

$$u_q^* - u_{qd}^* + (V_{dead}Dq)_d = 4V_{dead}\cos(\theta_e + \alpha) + u_{qh}. \tag{10b}$$

Since V_{dead} can be regarded as a constant at steady state, it can be extracted by the harmonic separation scheme introduced as follows:

Firstly, (10a) and (10b) multiplied by $\sin(\theta_e + \alpha)$ and $\cos(\theta_e + \alpha)$, respectively, will yield (11):

$$\begin{aligned} &\left[u_d^* - u_{dd}^* + (V_{dead}Dd)_d\right]\sin(\theta_e + \alpha) \\ &\quad = \left[4V_{dead}\sin(\theta_e + \alpha) + u_{dh}\right]\sin(\theta_e + \alpha) \end{aligned} \tag{11a}$$

$$\begin{aligned} &\left[u_q^* - u_{qd}^* + (V_{dead}Dq)_d\right]\cos(\theta_e + \alpha) \\ &\quad = \left[4V_{dead}\cos(\theta_e + \alpha) + u_{qh}\right]\cos(\theta_e + \alpha) \end{aligned} \tag{11b}$$

(11a) plus (11b) becomes:

$$\begin{aligned} &\left[u_d^* - u_{dd}^* + (V_{dead}Dd)_d\right]\sin(\theta_e + \alpha) \\ &\quad + \left[u_q^* - u_{qd}^* + (V_{dead}Dq)_d\right]\cos(\theta_e + \alpha) \\ &\quad = 4V_{dead} + u_{dh}\sin(\theta_e + \alpha) + u_{qh}\cos(\theta_e + \alpha). \end{aligned} \tag{12}$$

Finally, substituting (5) into (12) yields:

$$\begin{aligned} &\left[u_d^* - u_{dd}^* + (V_{dead}Dd)_d\right]Dd/4 \\ &\quad + \left[u_q^* - u_{qd}^* + (V_{dead}Dq)_d\right]Dq/4 \\ &\quad = 4V_{dead} + u_{dh}Dd/4 + u_{qh}Dq/4. \end{aligned} \tag{13}$$

Equation (13) is the key model for the extraction of V_{dead}, and the whole harmonic separation scheme can be illustrated by the control block diagram shown in Fig. 2. Its working principle is explained as follows:

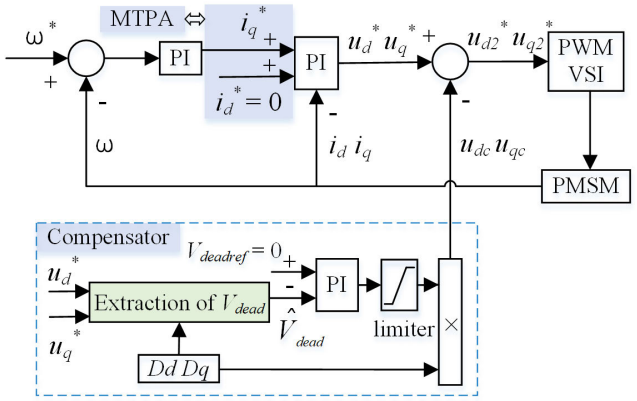

FIGURE 3. Proposed extraction and compensation of V_{dead} in a PMSM vector control system.

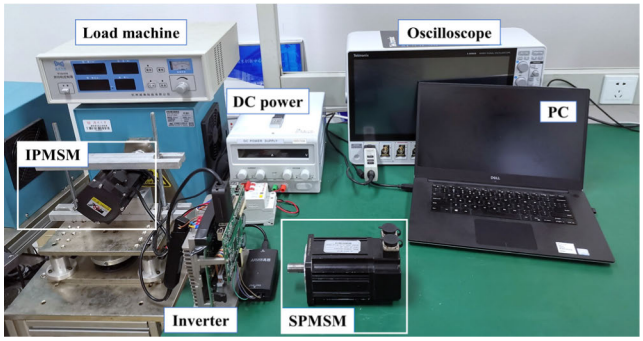

FIGURE 4. Prototype SPMSM, IPMSM and test rig.

In (13), Dd and Dq can be directly calculated by (3) and (4), while u_{dd}^*, u_{qd}^*, $(V_{dead}Dd)_d$ and $(V_{dead}Dq)_d$ can be obtained by low-pass filters, as shown in Fig. 2. The $4V_{dead}$ in (13) can be considered as a DC term. And for those low voltage/low speed PMSMs designed for servo control or high-accuracy actuators, the harmonics in u_{dh} and u_{qh} are quite negligible, especially in unsaturated region. Based on this hypothesis, it can be known that the two terms, $u_{dh}Dd/4$ and $u_{qh}Dq/4$, are both high-frequency harmonic terms. In short, as can be seen in (13), the expression on the left side consists of variables that are measurable, while the expression on the right side has a constant DC term $4V_{dead}$ and two high-order harmonic terms $u_{dh}Dd/4$ and $u_{qh}Dq/4$. Thus, the DC component V_{dead} in (13) can be directly extracted by the control block diagram illustrated in Fig. 2. Besides, $V_{dead}Dd$, $V_{dead}Dq$, u_d^*, u_q^* and the left side of (13) in Fig. 2 mainly contain 6th harmonic denoted by $6f_e$, and f_e is the fundamental frequency of machine operation. The cut-off frequency f_c of LPFs is set to $f_c = 0.1 \times 6f_e$. And a detailed description of LPFs and the extraction of V_{dead} at different cut-off frequencies are given in Appendix B.

III. FEEDBACK COMPENSATION SCHEME OF VSI NONLINEARITY

Once V_{dead} can be real-time extracted, disturbance voltage terms $V_{dead}Dd$ and $V_{dead}Dq$ can be online compensated afterwards [26], [28]. Since the disturbance voltage term V_{dead} can be considered as a constant at steady state, a PI control scheme of close-loop feedback is proposed for its compensation, as illustrated in Fig. 3. It can be seen in the control block diagram that the reference value of V_{dead} is set to 0V, which means that it will be eventually compensated to 0V. In this case, $V_{dead}Dd$ and $V_{dead}Dq$ will be consequently minimized to 0V, as a consequence, reference voltages and actual ones can be equivalent. As shown in Fig. 3, the PI output is multiplied by Dd and Dq, respectively, and their products u_{dc} and u_{qc} will be employed for the compensation of dq-axis disturbance voltages. Both u_{d2}^* and u_{q2}^* are the dq-axis reference voltages after compensation, and will be sent to the SVPWM control. In order to prevent over compensation under transient conditions, a saturation function is applied to limit the PI output. The limit can be determined according to the output peak of PI regulator at the rated current.

As can be seen from Fig. 1(a), it is note that the average value of Dd is zero under $i_d = 0$ control, which means that the DC component $(V_{dead}Dd)_d$ in (13) is also be zero. However, under $i_d \neq 0$ control, the DC component $(V_{dead}Dd)_d$ in (13) is not be zero and needs to be considered. The above mentioned variation in $(V_{dead}Dd)_d$ is a key factor in the harmonic analysis based compensation of VSI nonlinearity [22], whereas most existing researches cannot adapt to working under both $i_d = 0$ and $i_d \neq 0$ controls. Thus, two PMSMs designed for low-speed actuators, being salient pole and non-salient pole, respectively, will be employed for evaluating the performance of proposed method under $i_d = 0$ and $i_d \neq 0$ (selecting MTPA as an example), respectively. The main design parameters of two prototype PMSMs are listed in Table 2. For the SPMSM, it will operate under conventional $i_d = 0$ control while the IPMSM will operate under the conventional MTPA control mode being introduced by following equations: [32]

$$\begin{cases} i_d^* = \dfrac{-\psi_m + \sqrt{\psi_m^2 + 8\left(L_d - L_q\right)^2 I_S^2}}{4\left(L_d - L_q\right)} \\ i_q^* = \sqrt{I_S^2 - i_d^2} \end{cases} \tag{14}$$

where I_s is the stator current from the speed loop output.

IV. EXPERIMENTAL VERIFICATION

A. TEST RIG AND HARDWARE CONFIGURATION OF DRIVE SYSTEM

The proposed method is experimentally validated on the PMSM test rig shown in Fig. 4, in which two prototype PMSMs are employed for investigation, respectively. The DC link voltage of test rig is set to 60V. A magnetic powder brake is firstly employed as the external load of PMSMs, which has an accuracy in torque production and will be replaced by a DC load machine for the step test afterwards. The product model of employed power inverter module is FSBB30CH60F,

TABLE 2. Design parameters of tested PMSMS.

Parameters	SPMSM	IPMSM
Rated current	4.5A	4.2A
Rated speed	600r/min	600r/min
Rated torque	2.4N·m	2.4N·m
Number of pole pairs	4	5
Nominal d-axis inductance	2.8mH	7.1mH
Nominal q-axis inductance	2.8mH	10.7mH
Permanent magnet flux linkage	109.1mWb	55.6mWb
Stator winding resistance	1.86Ω	0.95Ω

TABLE 3. Design parameters of employed VSI.

Parameters	Typical value
Turn-on delay (T_{on})	0.49μs
Turn-off delay (T_{off})	0.86μs
Dead time (T_{dead})	3μs
Switching period (T_s)	83.3μs
Voltage drop of the switching tube (V_{sat})	2.75V
Voltage drop of the freewheeling diode (V_d)	2.4V

Note: Design parameters cited from data sheet of FSBB30CH60F

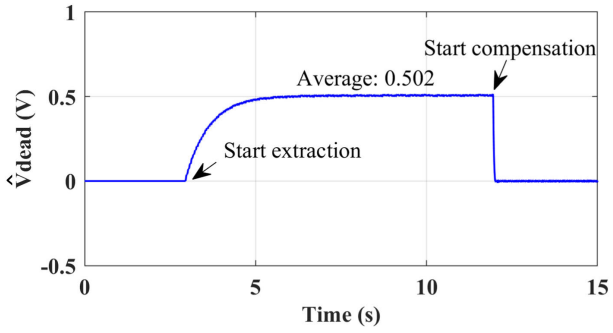

FIGURE 5. Extraction and compensation of V_{dead} under $i_d = 0$ control (150r/min and 1.5N·m).

of which typical electrical characteristic parameters are listed in Table 3. Besides, the control board and the power board are integrated together, and the product model of employed microprocessor is MKV31F256VLL12 being of ARM architecture whose ADC resolution is 16bits. According to the technical information of power inverter module, the switching frequency of inverter is set to 12kHz and the dead time is set to 3μs.

B. TEST RESULTS OF SPMSM UNDER $i_d = 0$

In order to test the performance of proposed method under $i_d = 0$ control, it is firstly employed on the drive control of the non-salient pole SPMSM. Fig. 5 shows the extraction and compensation of V_{dead} under $i_d = 0$ control when load torque is 1.5N·m. It can be seen that the proposed extraction scheme has a good performance in convergence, and afterwards, the extracted disturbance voltage term V_{dead} can be minimized to 0V. After the settling down of compensation, disturbance voltages in u_d^* and u_q^* would be eventually minimized to zero, which implies a good application potential in advanced drive controls such as sensorless control [18]–[20], predictive current control [5], [38], and parameter identification [21], [22], thanks to its parameter-independent features. It is worth noting that the extracted V_{dead} increases with the increase of load torque, which indicates that the proposed method recognizes the variation of voltage drops of power devices without offline experiments.

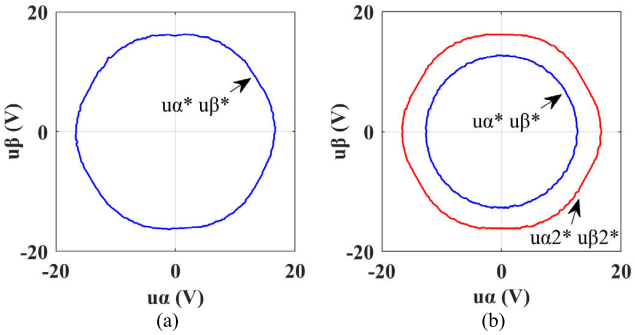

FIGURE 6. $\alpha\beta$-axis reference voltages under $i_d = 0$ control (150r/min, 1.5N·m). (a) and (b) are without and with proposed compensation.

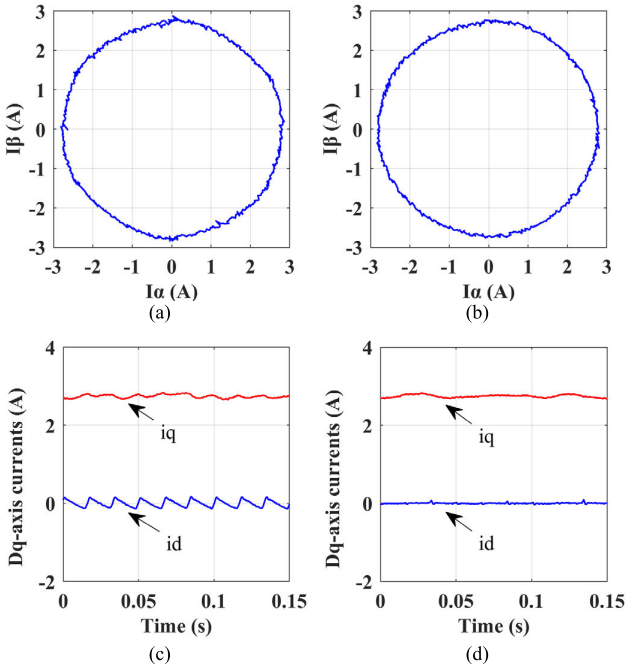

FIGURE 7. $\alpha\beta$-axis currents and dq-axis currents under $i_d = 0$ control (150r/min, 1.5N·m). (a) and (c) are without compensation while (b) and (d) are with proposed compensation.

In Fig. 6, u_α^* and u_β^* are $\alpha\beta$-axis reference voltages obtained by inverse Park-transformation of u_d^* and u_q^* under $i_d = 0$ control, while $u_{\alpha 2}^*$ and $u_{\beta 2}^*$ are $\alpha\beta$-axis voltages obtained by inverse Park-transformation of u_{d2}^* and u_{q2}^*, as detailed in Fig. 3. Obviously, the synthesized voltage vector of u_α^* and u_β^* becomes more circular with the proposed compensation, which indicates that the real stator winding voltages would have less harmonics after compensation [2]. Similarly, as can be seen in Fig. 7, the current vector in $\alpha\beta$-axis coordinate

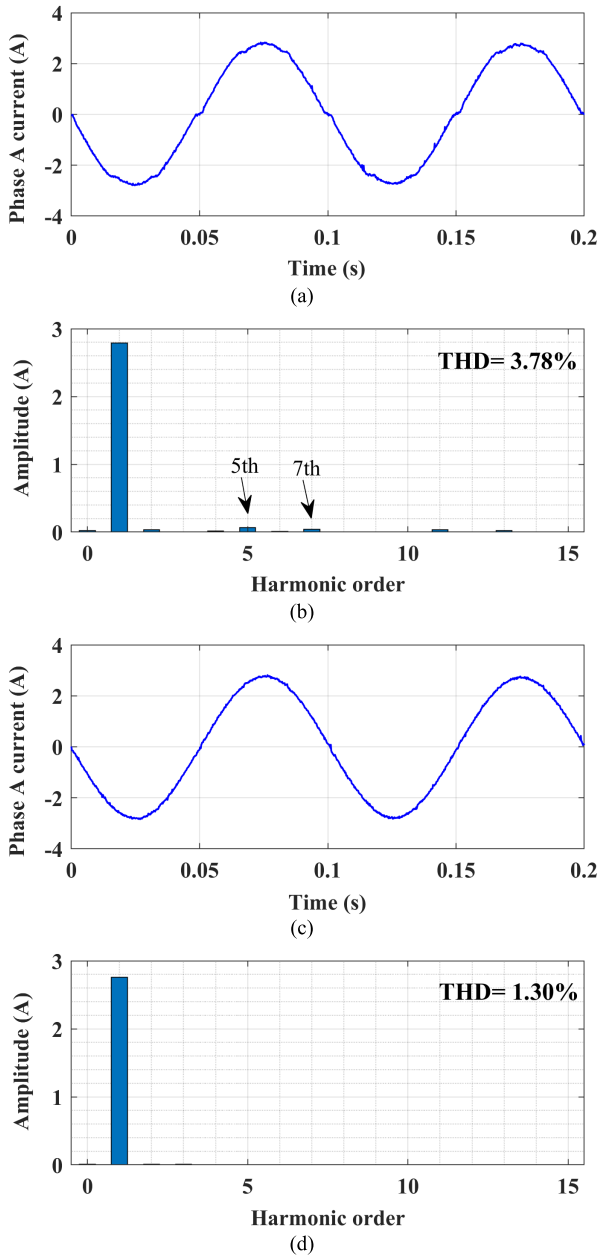

FIGURE 8. Phase A current and FFT analysis under $i_d = 0$ control (150r/min, 1.5N·m). (a) and (b) are without compensation while (c) and (d) are with proposed compensation.

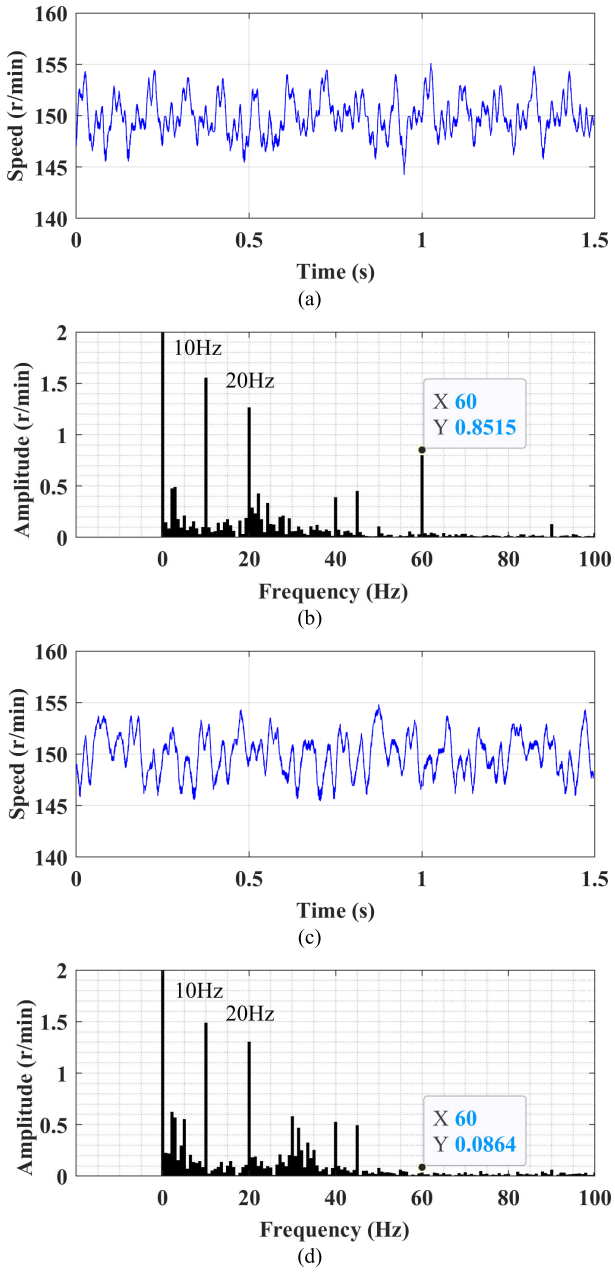

FIGURE 9. Rotor speed and FFT analysis under $i_d = 0$ control (1.5N·m, 150r/min). (a) and (b) are without compensation while (c) and (d) are with proposed compensation.

becomes more circular after the compensation and the waveforms of *dq*-axis currents become much smoother, which is quite important in the reduction of torque ripples. Besides, as shown in Fig. 8, the clamping phenomenon during the zero-crossing becomes negligible, and the current of phase A is almost sinusoidal after the proposed compensation. The FFT results shown in Figs. 8(b) and (d) confirms that the 5th and 7th harmonics are almost zero after the compensation.

Fig. 9 shows the waveforms of rotor speed with and without the proposed compensation, together with their FFT results, respectively. In Fig. 9, 10Hz is the fundamental frequency of three-phase currents. The 20Hz component is mainly related to the scaling error in current measurement [33], while the 60Hz component is mainly caused by the VSI nonlinearity. It can be seen in Fig. 9 that after the proposed compensation, the 6th harmonic in rotor speed can be significantly suppressed. As a consequence, torque ripples would be therefore suppressed [34].

Furthermore, as can be clearly seen in Fig. 6(b), the disturbance voltage due to VSI nonlinearity will result in a significant distortion in the reference voltage, especially at relatively low-speed region, for example, 150r/min. There-

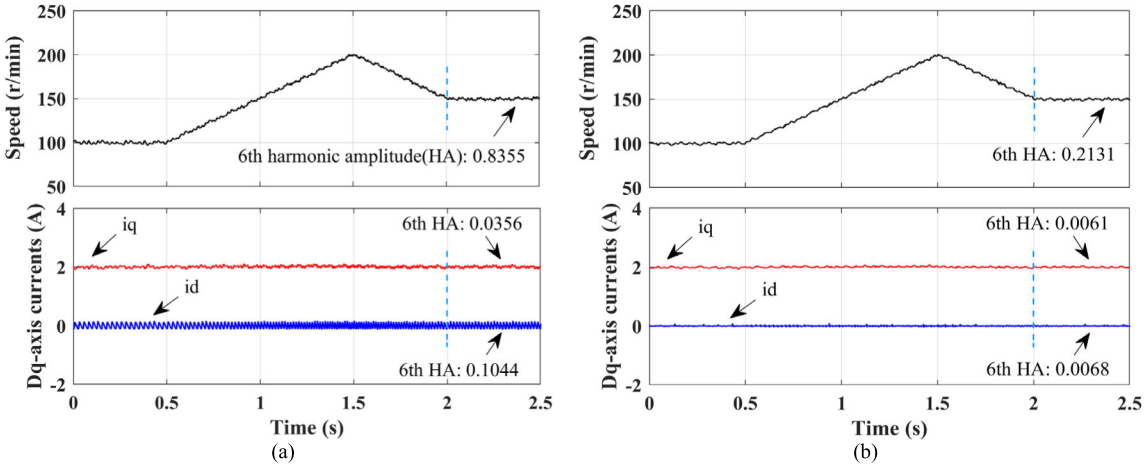

FIGURE 10. Measured rotor speed and *dq*-axis currents during speed ramp response (1.0N·m). (a) Without proposed compensation. (b) With proposed compensation.

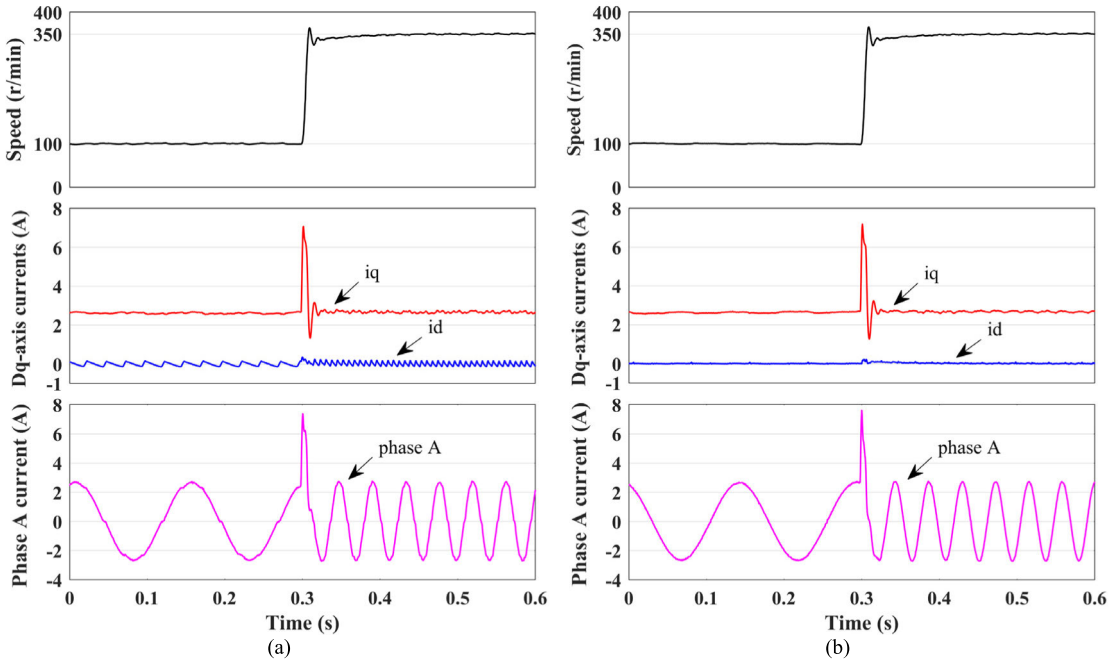

FIGURE 11. Measured rotor speed, *dq*-axis and phase A currents during speed step response from 100r/min to 350r/min (1.5N·m). (a) Without proposed compensation. (b) With proposed compensation.

fore, the compensation of disturbance voltages is quite essential in reality, especially in a low-speed actuator system which works at relatively low voltage and is sensitive to current and voltage harmonics. Besides, in high speed applications such as the flux weakening control, the compensation of VSI nonlinearity is also important for achieving a higher speed expansion and a larger constant output power region [35].

C. DYNAMIC TEST ON SPMSM UNDER $i_d = 0$

In Figs. 10-12, the dynamic performance of proposed method is further evaluated on a non-salient pole SPMSM, by way of speed ramp/step response and load step response, respectively. Fig. 10 shows measured *dq*-axis currents and rotor speeds under variable speed control. The ramp response of rotor speed is at the rate of 100r/s. It can be seen in Fig. 10(a) that the 6th harmonic oscillations in *d*-axis current is quite obvious during the whole test, while those oscillations could be significantly suppressed within $\pm$ 0.05A after the proposed compensation. It is also noteworthy that small 6th harmonic oscillations in *q*-axis current and rotor speed can be also minimized after the proposed compensation.

Fig. 11 shows measured waveforms during the step response of rotor speed. It can be seen that with the proposed compensation, the measured currents have quite negligible 6th harmonic during the whole step response test. Fig. 12 shows measured waveforms during the load step

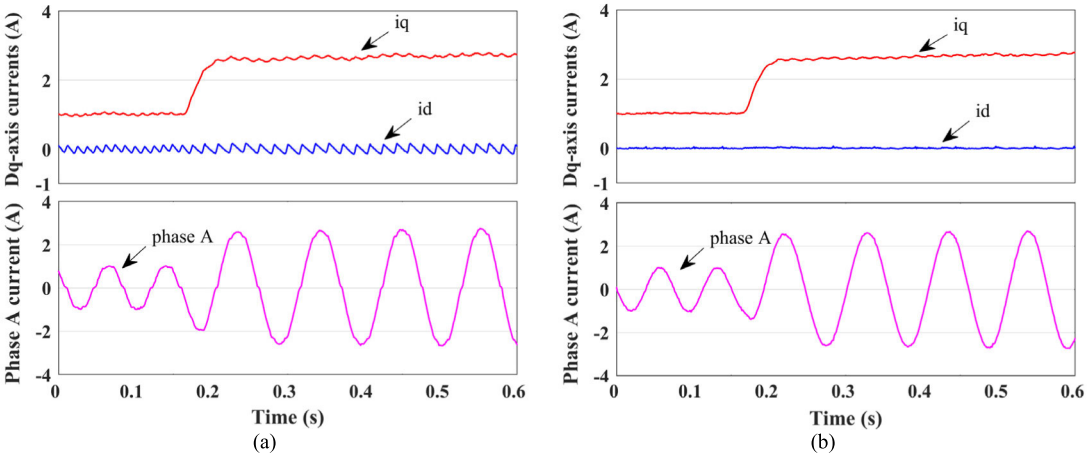

FIGURE 12. Measured *dq*-axis and phase currents during load step response, from 0.5N·m to 1.4N·m (200r/min). (a) Without proposed compensation. (b) With proposed compensation.

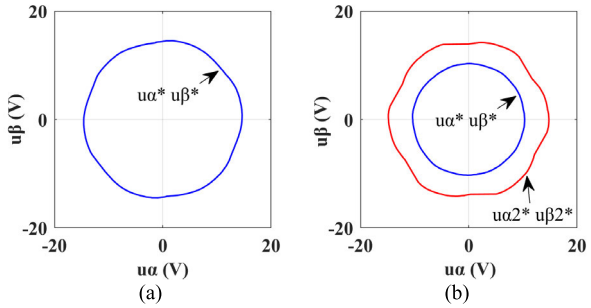

FIGURE 13. Measured vector trajectory of $\alpha\beta$-axis reference voltages under MTPA control (200r/min, 1.5N·m). (a) Without proposed compensation. (b) Comparison between compensated (in blue) and uncompensated (in red) voltage trajectories.

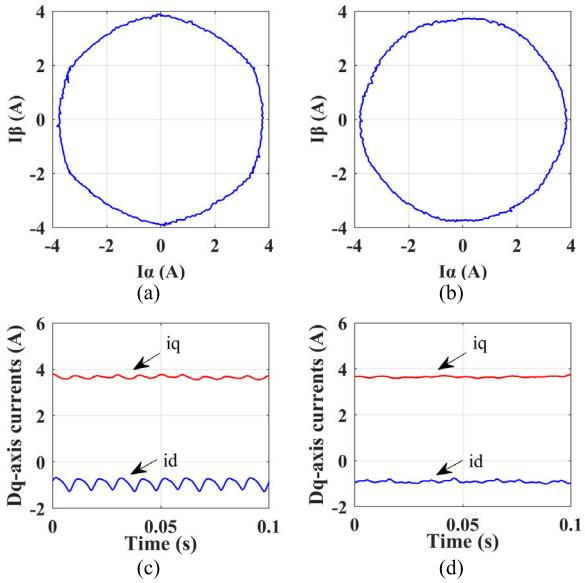

FIGURE 14. $\alpha\beta$-axis and *dq*-axis currents under MTPA control (200r/min, 1.5N·m). (a) and (c) are without compensation while (b) and (d) are with proposed compensation.

response. As a result, the *q*-axis current will immediately increase from 1A to 2.7A after the addition of external load from 0.5N·m to 1.4N·m. In Fig. 12(a), 6th harmonic in

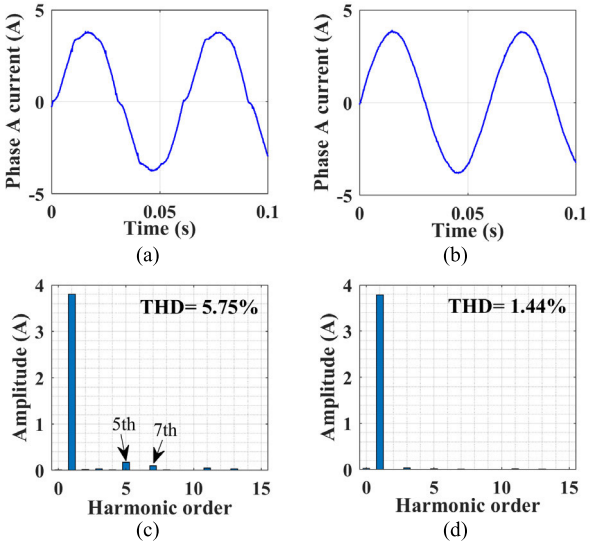

FIGURE 15. Measured phase A current and FFT analysis under MTPA control (200r/min, 1.5N·m). (a) and (c) are without compensation while (b) and (d) are with proposed compensation.

dq-axis currents and clamping effect during the zero-crossing transients are quite obvious without compensation, whereas those phenomena will be eliminated with the proposed compensation. Based the above tests and analysis, it can be concluded that the proposed method can achieve a continuous accurate compensation under both dynamic and steady state tests.

D. TEST RESULTS OF IPMSM UNDER MTPA CONTROL

In order to verify the effectiveness of proposed method under $i_d \neq 0$ control, a prototype IPMSM operating under MTPA control (14) is employed for performance evaluation, and relevant experimental results and FFT analysis are depicted in Figs. 13-15.

In Fig. 13, it is obvious that the rotation of voltage vector in $\alpha\beta$-axis coordinate becomes more circular with the proposed

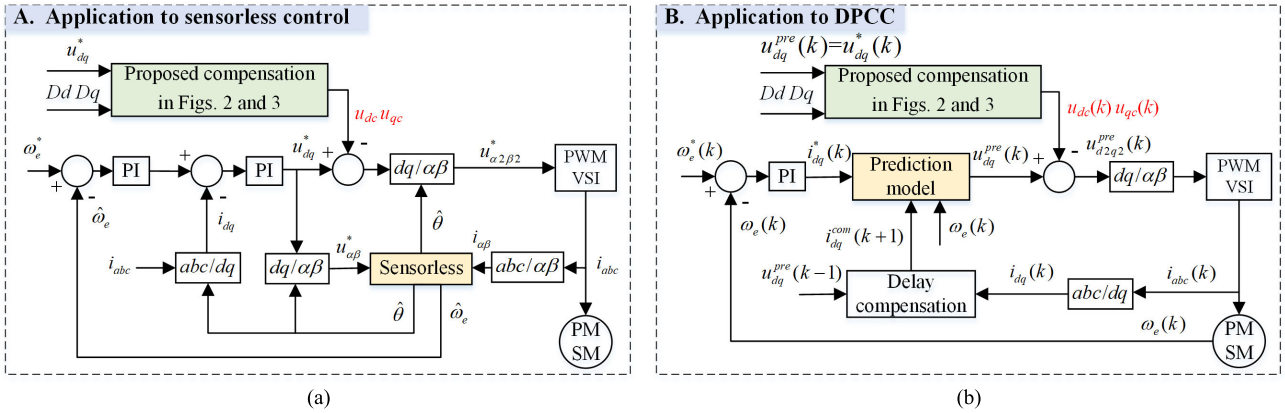

FIGURE 16. Application of proposed method to state observation controls. (a). Compensation for sensorless control. (b). Compensation for DPCC.

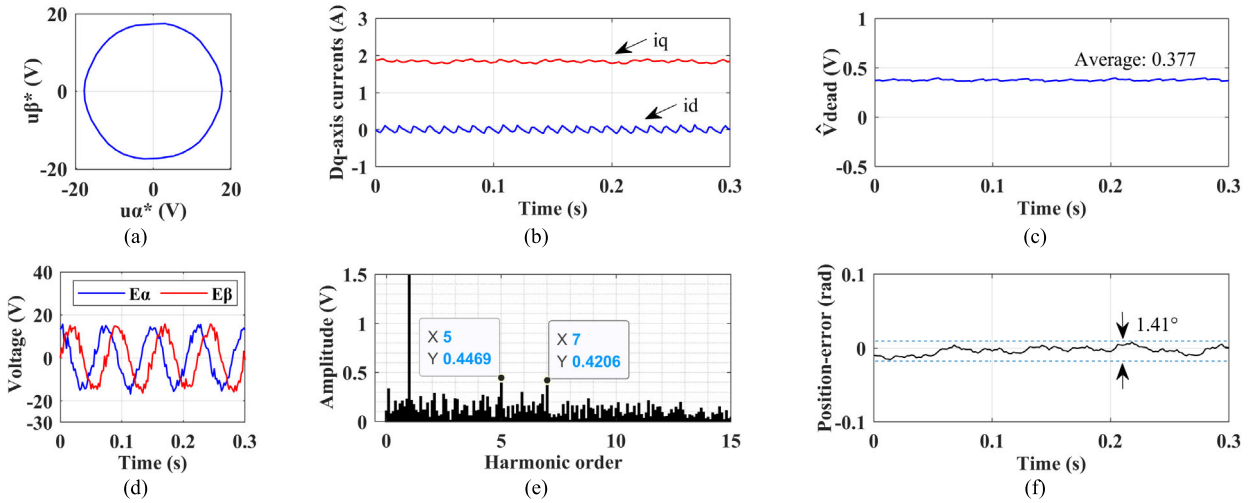

FIGURE 17. Experimental results without compensation of VSI nonlinearity (T_{dead} = 2μs, 200r/min, 1N·m). (a) Voltage vector trajectory. (b) *dq*-axis currents. (c) Extracted V_{dead}. (d) Estimated back EMF. (e) FFT results of E_α. (f) Position-error between measured and estimated rotor positions.

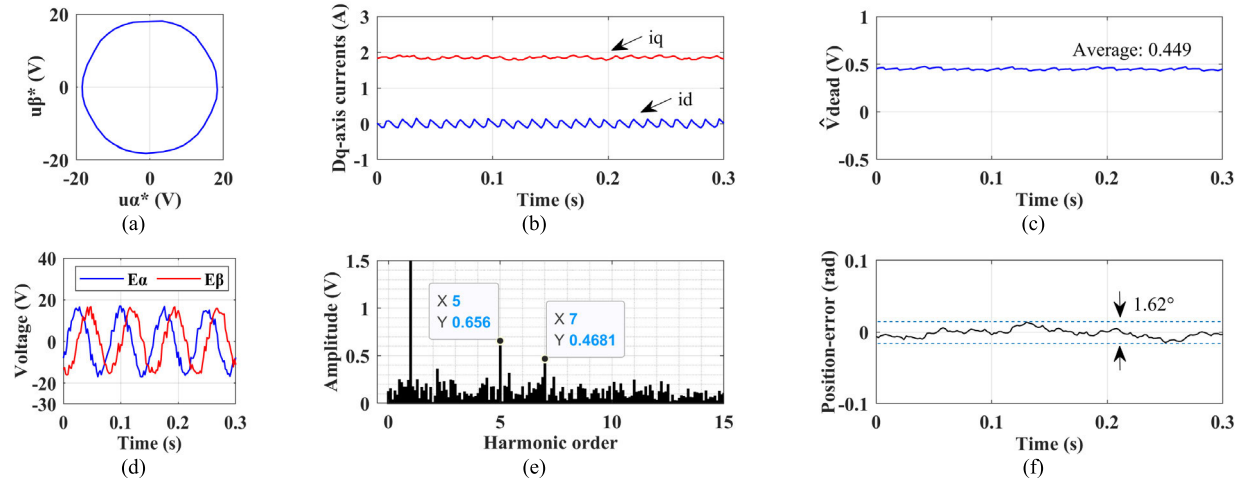

FIGURE 18. Experimental results without compensation of VSI nonlinearity (T_{dead} = 3μs, 200r/min, 1N·m). (a) Voltage vector trajectory. (b) *dq*-axis currents. (c) Extracted V_{dead}. (d) Estimated back EMF. (e) FFT results of E_α. (f) Position-error between measured and estimated rotor positions.

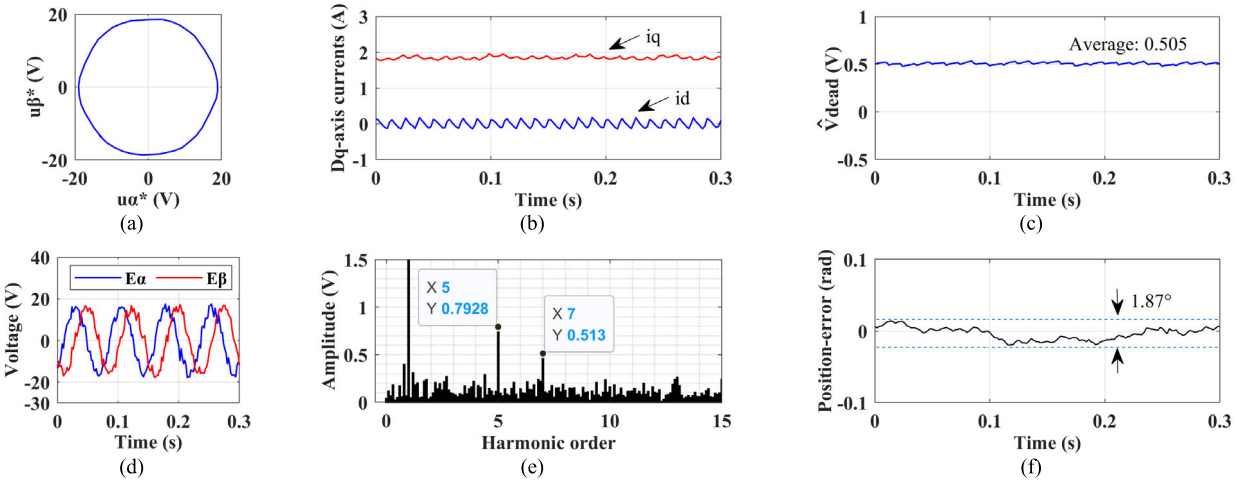

FIGURE 19. Experimental results without compensation of VSI nonlinearity ($T_{dead} = 4\mu s$, 200r/min, 1N·m). (a) Voltage vector trajectory. (b) dq-axis currents. (c) Extracted V_{dead}. (d) Estimated back EMF. (e) FFT results of E_α. (f) Position-error between measured and estimated rotor positions.

compensation. And in Fig. 14, with the proposed compensation, the rotation of current vector in $\alpha\beta$-axis coordinate becomes more circular, and the dq-axis currents become quite smooth. It is worth noting that compared with $i_d = 0$ control, the 6th harmonic in q-axis current will become more significant, which can be explained that the current angle λ has been changed to non-zero under $i_d \neq 0$ control, as described in Table 1. Besides, as can be seen in Fig. 15, the phase A current is almost sinusoidal and its total harmonic distortion (THD) is significantly reduced from 5.75% to 1.44% after the compensation. From the above test results and analyses, it manifests that the proposed scheme also has excellent performance under $i_d \neq 0$ control, which confirms the theory proposed in section II and Fig. 3.

V. APPLICATION OF PROPOSED METHOD TO STATE OBSERVATION CONTROL OF PMSM

As mentioned hereinbefore, conventional state observation controls, such as model-based sensorless control and DPCC, needs accurate reference voltages and/or less-harmonic stator currents to observe rotor position/speed, stator current and so on. However, due to the VSI nonlinearity, the reference voltages and measured stator currents usually have non-negligible harmonics. Since the proposed method is parameter-independent and needs few CPU calculation and no additional hardware, it is inherently proper for improving the performance of state observation controls. Thus, the application of proposed method will be studied in this section, and the SPMSM introduced in Table 2 will be employed for tests. Block diagrams of application of proposed method including PMSM-model-based sensorless control and DPCC are shown in Fig. 16. In Fig. 16(a), the sensorless strategy is based on the conventional sliding mode observer (SMO) and phase-locked loop (PLL), whose detailed design process is introduced in Appendix C. In Fig. 16(b), the prediction model of investigated DPCC is cited from [38], which is introduced in Appendix D.

A. EXAMPLE 1: APPLICATION OF PROPOSED METHOD TO SENSORLESS CONTROL

In traditional SMO-based sensorless control, the $\alpha\beta$-axis voltage equations can be expressed as follows: [36], [37]

$$\begin{cases} \begin{bmatrix} u_\alpha \\ u_\beta \end{bmatrix} = \begin{bmatrix} R_s + pL_s 0 \\ 0 R_s + pL_s \end{bmatrix} \begin{bmatrix} i_\alpha \\ i_\beta \end{bmatrix} + \begin{bmatrix} E_\alpha \\ E_\beta \end{bmatrix} \\ \begin{bmatrix} E_\alpha \\ E_\beta \end{bmatrix} = \omega_e \psi_m \begin{bmatrix} -\sin\theta \\ \cos\theta \end{bmatrix} \end{cases} \tag{15}$$

where u_α and u_β are actual $\alpha\beta$-axis voltages, i_α and i_β are $\alpha\beta$-axis currents, L_s is the stator inductance ($L_s = L_d = L_q$), p is the differential operator, E_α and E_β are the extended back EMF.

Usually, the real machine voltages u_α and u_β are not measurable due to the high frequency PWM, and $\alpha\beta$-axis reference voltages u_α^* and u_β^* are employed for replacing u_α and u_β in control algorithms. However, u_α^* and u_β^* contain obvious harmonic components resulted from VSI nonlinearity, and so do i_α and i_β, which are employed as the inputs of SMO. Thus, the performance of sensorless control will deteriorate owing to the harmonics in input signals.

Considering the distorted voltage due to VSI nonlinearity, and neglecting the influence of cross-coupling effect, the $\alpha\beta$-axis voltage equations can be written as follows:

$$\begin{bmatrix} u_\alpha^* \\ u_\beta^* \end{bmatrix} = \begin{bmatrix} R_s + pL_s & 0 \\ 0 & R_s + pL_s \end{bmatrix} \begin{bmatrix} i_\alpha \\ i_\beta \end{bmatrix} + \begin{bmatrix} E_\alpha \\ E_\beta \end{bmatrix} + \begin{bmatrix} \cos(\theta) & -\sin(\theta) \\ \sin(\theta) & \cos(\theta) \end{bmatrix} \begin{bmatrix} V_{dead} Dd \\ V_{dead} Dq \end{bmatrix}. \tag{16}$$

As shown in (16), it is essential to compensate the VSI nonlinearity to ensure the accuracy of u_α^* and u_β^*. Otherwise,

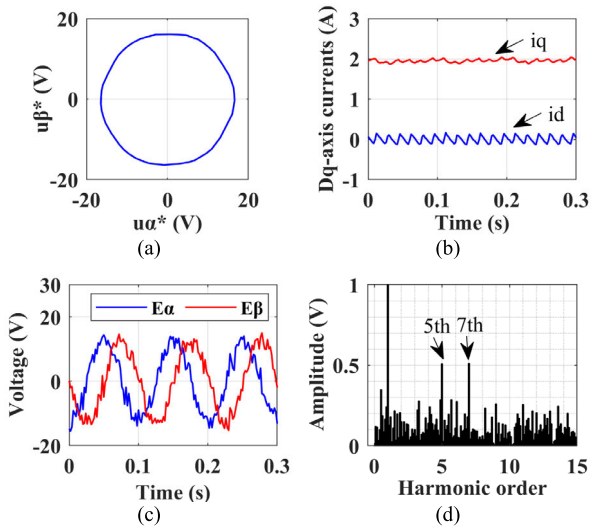

FIGURE 20. Experimental results without compensation of VSI nonlinearity ($T_{dead} = 3\mu s$, 150r/min, 1N·m). (a) Voltage vector trajectory. (b) *dq*-axis currents. (c) Estimated back EMF. (d) FFT results of E_α.

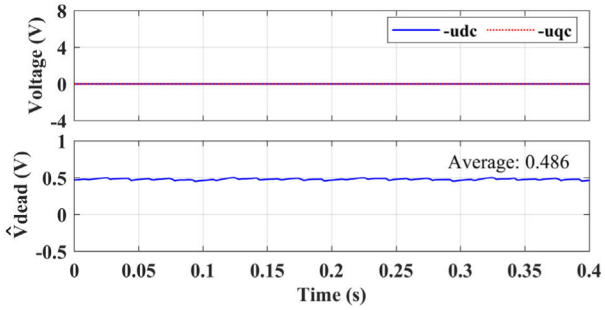

FIGURE 21. Initial value of feedback compensation voltages (u_{dc} and u_{qc}) and online extracted V_{dead} before compensation.

the performance of sensorless control will deteriorate due to those nolinearities. Figs. 17-19 are test results using sensorless control without VSI nonlinearity compensation under $T_{dead} = 2\mu s$, $3\mu s$ and $4\mu s$, respectively. As the dead time increases, the 5th and 7th harmonics of u_α^*, u_β^*, i_α, i_β, and the value of extracted V_{dead} increase. As a result, the estimated back EMF will contain more 5th and 7th harmonics with the increase of dead time. As a consequence, the back EMF harmonics will increase the position-error in the PLL based position observation, as shown in Figs. 17-19(f).

On condition that the rotor speed and dead time are set to 150r/min and $3\mu s$, respectively, Figs. 20-23 are test results without compensation of VSI nonlinearity, while Figs. 24-27 are waveforms with the proposed compensation. In Fig. 20, the estimated E_α has obvious 5th and 7th harmonics due to the influence of VSI nonlinearity. Comparing Fig. 20(d) with Fig. 24(d), it is evident that the proposed method can effectively reduce both 5th and 7th harmonics in estimated back EMF. Besides, the extracted V_{dead} will quickly converge to 0V after the proposed compensation, as shown in Fig. 25. Comparing Fig. 22 with Fig. 26,

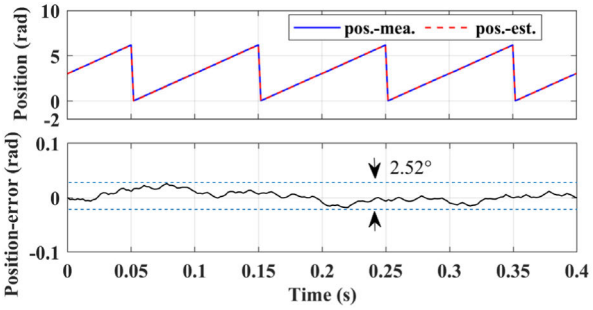

FIGURE 22. Error between measured and estimated rotor positions without compensation of VSI nonlinearity ($T_{dead} = 3\mu s$, 150r/min, 1N·m).

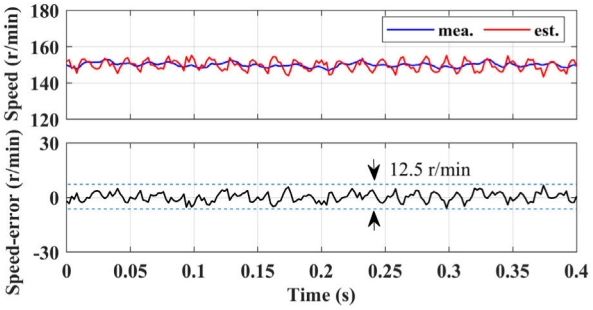

FIGURE 23. Error between measured and estimated rotor speeds without compensation of VSI nonlinearity ($T_{dead} = 3\mu s$, 150r/min, 1N·m).

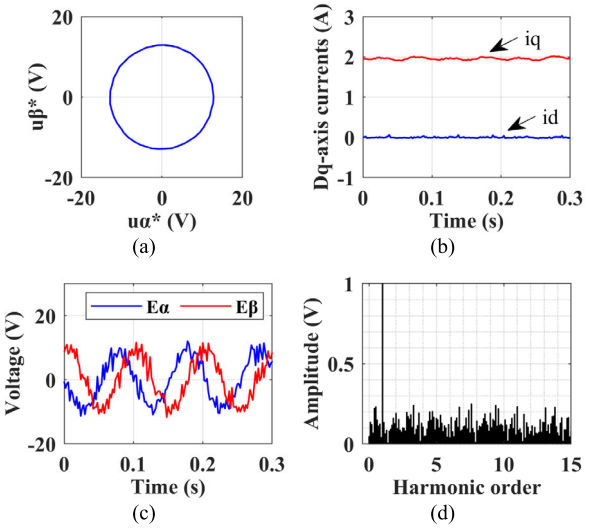

FIGURE 24. Experimental results with proposed compensation ($T_{dead} = 3\mu s$, 150r/min, 1N·m). (a) Voltage vector trajectory. (b) *dq*-axis currents. (c) Estimated back EMF. (d) FFT results of E_α.

it can be seen that the maximum position-error will distinctly decreases with the proposed compensation, which decreases from 2.52° to 1.12°. In addition, as shown in Figs. 23 and 27, the oscillation of observed rotor speed is also significantly reduced with the proposed compensation, whose peak-to-peak error decreases from 12.5r/min to 10.1r/min.

B. EXAMPLE 2: APPLICATION OF PROPOSED METHOD TO DPCC

The conventional DPCC can directly obtain the voltage vector via. PMSM model, which guarantees the current loop can

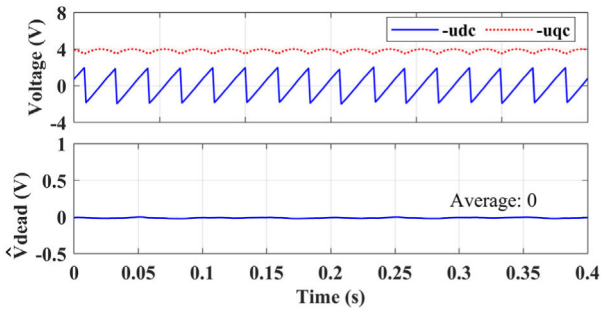

FIGURE 25. Feedback compensation voltages (u_{dc} and u_{qc}) added to outputs of PI regulators and online extracted V_{dead} after compensation.

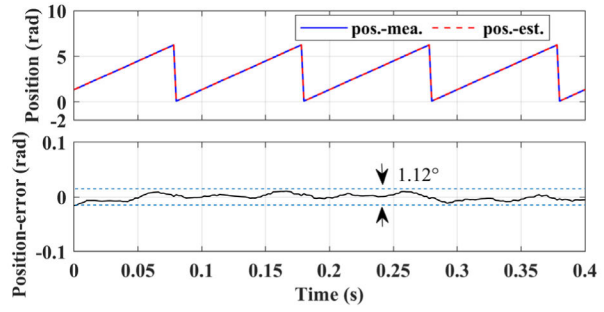

FIGURE 26. Error between measured and estimated rotor positions with proposed comp. of VSI nonlinearity ($T_{dead} = 3\mu s$, 150r/min, 1N·m).

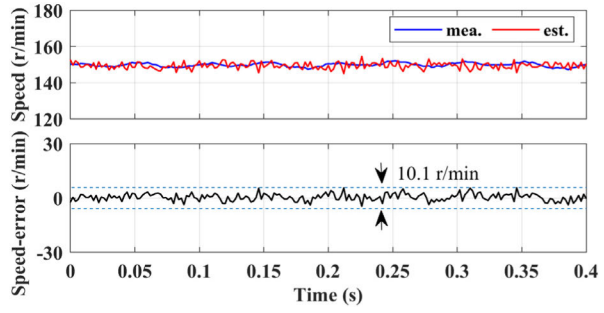

FIGURE 27. Error between measured and estimated rotor speeds with proposed compensation of VSI nonlinearity ($T_{dead} = 3\mu s$, 150r/min, 1N·m).

achieve good dynamic and steady characteristics at the same time. As detailed in Appendix D, the conventional DPCC model does not consider the influence of VSI nonlinearity in predicted dq-axis voltages: [38]

$$\begin{cases} u_d^{pre}(k) = R_s i_d^{com}(k+1) + (L_d/T) \\ \qquad \times \left[i_d^*(k) - i_d^{com}(k+1)\right] \\ \qquad -\omega_e L_q i_q(k) \\ u_q^{pre}(k) = R_s i_q^{com}(k+1) + \left(L_q/T\right) \\ \qquad \times \left[i_q^*(k) - i_q^{com}(k+1)\right] \\ \qquad +\omega_e L_d i_d^{com}(k+1) + \omega_e \psi_m \end{cases} \tag{17}$$

where k denotes the kth sampling period.

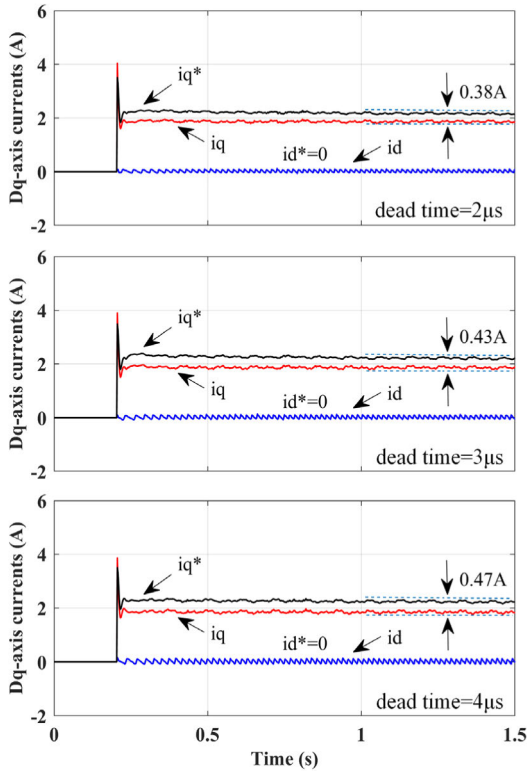

FIGURE 28. dq-axis reference and measured currents of DPCC without compensation of VSI nonlinearity ($T_{dead} = 2\mu s$, $3\mu s$ and $4\mu s$, 1N·m).

The predicted dq-axis voltages $u_d^{pre}(k)$ and $u_q^{pre}(k)$ are used as reference voltages for the SVPWM control. However, as discussed in Section II, the reference and output voltages are usually not exactly the same due to the existence of VSI nonlinearity. $u_d^{pre}(k)$ and $u_q^{pre}(k)$ considering the VSI nonlinearity can be re-written as follows:

$$\begin{cases} u_d^{pre}(k) = R_s i_d^{com}(k+1) + (L_d/T) \\ \qquad \times \left[i_d^*(k) - i_d^{com}(k+1)\right] \\ \qquad -\omega_e L_q i_q(k) + V_{dead} Dd(k) \\ u_q^{pre}(k) = R_s i_q^{com}(k+1) + \left(L_q/T\right) \\ \qquad \times \left[i_q^*(k) - i_q^{com}(k+1)\right] \\ \qquad +\omega_e L_d i_d^{com}(k+1) + \omega_e \psi_m + V_{dead} Dq(k). \end{cases} \tag{18}$$

According to the Table 1, assuming that the value of V_{dead} is 0.5V and $i_d = 0$, the term $V_{dead}Dd(k)$ mainly contains 6th harmonic and its average value will be 0V while the value of $V_{dead}Dq(k)$ is approximately 2V. Since the back EMF is relatively small at low-speed, the term $V_{dead}Dq(k)$ will have great influence on the current loop control, in which the tracking performance of feedback current will deteriorate. Thus, it is necessary to take into account the compensation of VSI nonlinearity for DPCC. Fig. 16(b) is the block diagram of DPCC using the proposed method. It should be noteworthy that with the proposed method, the predicted $u_d^{pre}(k)$ and

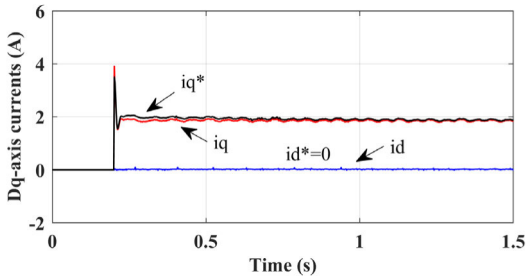

FIGURE 29. *dq*-axis reference and measured currents of DPCC with proposed compensation of VSI nonlinearity ($T_{dead} = 3\mu s$, 1N·m).

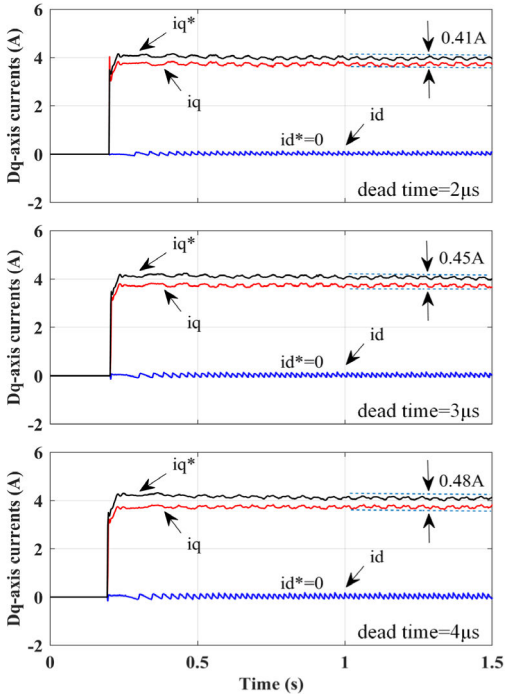

FIGURE 30. *dq*-axis reference and measured currents of DPCC without compensation of VSI nonlinearity ($T_{dead} = 2\mu s$, $3\mu s$ and $4\mu s$, 2N·m).

$u_q^{pre}(k)$ shown in Fig. 16(b) are equivalent to the reference voltages u_d^* and u_q^* shown in Fig. 3.

Fig. 28 shows the experimental results of DPCC without compensation of VSI nonlinearity under $T_{dead} = 2\mu s$, $3\mu s$ and $4\mu s$, respectively. In Fig. 28, the measured i_q cannot accurately track the corresponding reference current i_q^*. When the dead time is set to $2\mu s$, $3\mu s$ and $4\mu s$, respectively, the steady-state error will be 0.38A, 0.43A and 0.47A, respectively. Obviously, the tracking ability of stator current deteriorates with the increase of dead time. This can be explained that the term $V_{dead}Dq(k)$ takes a non-negligible portion of q-axis reference voltage, and i_q^* cannot accurately matches i_q. Since $V_{dead}Dd(k)$ is of zero mean under $i_d = 0$ control, i_d will fluctuate around i_d^* and contains obvious 6th harmonic component, as shown in Fig. 28.

Fig. 29 shows the application of proposed method to the DPCC. It can be seen that the DPCC with the proposed

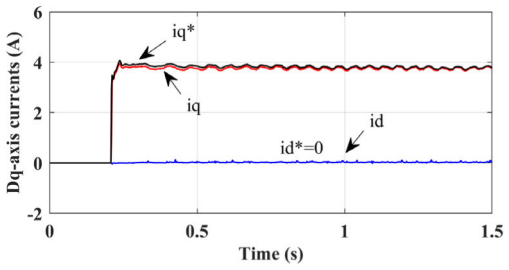

FIGURE 31. *dq*-axis reference and measured currents of DPCC with proposed compensation of VSI nonlinearity ($T_{dead} = 3\mu s$, 2N·m).

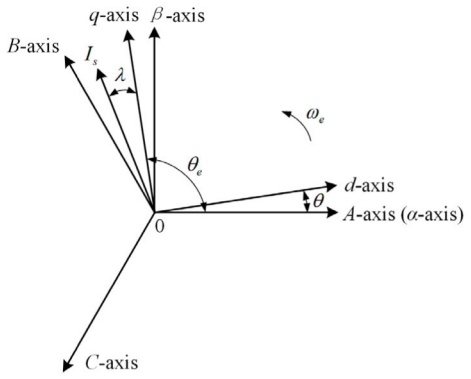

FIGURE 32. Relation diagram of three coordinates in this paper.

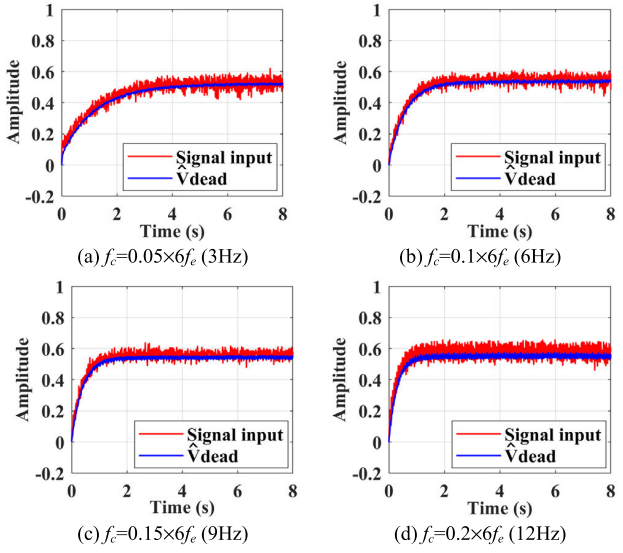

FIGURE 33. Extraction of V_{dead} at different cut-off frequencies.

compensation can accurately track the reference currents i_q^* and i_d^*, and significantly reduces the oscillation of i_d and i_q.

Fig. 30 shows the test results of DPCC without compensation of VSI nonlinearity under $T_{dead} = 2\mu s$, $3\mu s$ and $4\mu s$, respectively, while Fig. 31 shows the DPCC with the proposed compensation under $T_{dead} = 3\mu s$. It can be seen that when $T_{dead} = 2\mu s$, $3\mu s$ and $4\mu s$, respectively, the steady-state error becomes 0.41A, 0.45A and 0.48A, respectively.

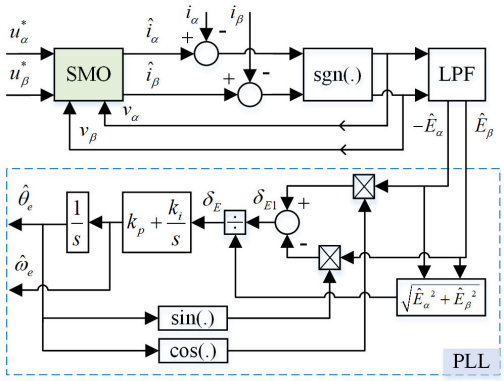

FIGURE 34. Sensorless control based on SMO and PLL.

It can be concluded that the steady-state error between $i* q$ and i_q increases with the dead time. In addition, since the overall distorted voltage due to VSI nonlinearity will increase with the current, it can be seen in Figs. 28 and 30 that the increase of load torque will increase the steady-state error. It also can be seen in Fig. 31 that the proposed compensation can significantly reduce the steady-state error and improve the tracking performance of dq-axis currents.

VI. CONCLUSION

A simple and parameter-independent compensation of VSI nonlinearity has been proposed in this paper, which is based on the cooperation of a harmonic separation scheme and a PI feedback. Compared with existing methods, the proposed scheme does not need extra hardware, system parameters, and can be used in both $i_d = 0$ and $i_d \neq 0$ controls. Its dynamic and steady state performances are evaluated on a non-salient pole SPMSM and a salient pole IPMSM, respectively, which shows good performances during the speed ramp/step response and load step response. Besides, the experiments show that the proposed method has a good application prospect in state observation controls such as the conventional sensorless control and DPCC. It is worth noting that, for electrical machines usually working under saturated regions or with quite significant cogging torque, an over compensation on the 6th harmonics will probably occur. In this case, an offline test for the 6th harmonics in back EMF and cogging torque will be needed for improving the accuracy of proposed method. It will be our future work to investigate the above challenge.

APPENDIX A

In this study, the relationships among abc, $\alpha\beta$ and dq coordinates are shown in Fig. 32.

APPENDIX B. SETUP OF CUT-OFF FREQUENCIES OF LOW-PASS FILTERS

The digital LPFs used in Fig. 2 are discretized from the first-order RC LPFs. The expression after discretization is:

$$u_o(k) = u_o(k-1) + 2\pi T f_c (u_i(k) - u_o(k-1)) \quad \text{(B1)}$$

where u_o is the signal output; u_i is the signal input; f_c is the cut-off frequency; T is the sampling period ($T = 83.3\mu s$).

Fig. 33 shows the extraction of V_{dead} at different cut-off frequencies when the f_e is 10Hz. With the increasing of f_c, the convergence speed can be improved while the steady-state fluctuation will synchronously rise up. The f_c has no influence on the average value of extracted V_{dead}, However, it will influence on the dynamic performance of extraction of V_{dead}, for example, the convergence speed and peak to peak oscillation at steady state. After a tradeoff between filtering effect and convergence speed, $f_c = 0.1 \times 6f_e$ is set as the employed f_c in principle during the whole speed range.

APPENDIX C. DESIGN PRINCIPLE OF SMO AND PLL

The $\alpha\beta$-axis state equations of SPMSM including the extended back EMF can be expressed as follows: [4], [36]

$$\frac{d}{dt}\begin{bmatrix} i_\alpha \\ i_\beta \end{bmatrix} = \frac{1}{L_s}\begin{bmatrix} -R_s & 0 \\ 0 & -R_s \end{bmatrix}\begin{bmatrix} i_\alpha \\ i_\beta \end{bmatrix} + \frac{1}{L_s}\begin{bmatrix} u_\alpha \\ u_\beta \end{bmatrix} - \frac{1}{L_s}\begin{bmatrix} E_\alpha \\ E_\beta \end{bmatrix}. \quad \text{(C1)}$$

In practical applications, the values of u_α and u_β are acquired from u_α^* and u_β^* in Fig. 16(a), respectively. It is noted that, after the compensation of VSI nonlinearity, u_α^* and u_β^* basically have no harmonic components. The EMF-based SMO is insensitive to parameter variation and converges rapidly, which is usually constructed as

$$\begin{cases} \dfrac{\mathrm{d}}{\mathrm{d}t}\begin{bmatrix} \hat{i}_\alpha \\ \hat{i}_\beta \end{bmatrix} = \dfrac{1}{L_s}\begin{bmatrix} -R_s & 0 \\ 0 & -R_s \end{bmatrix}\begin{bmatrix} \hat{i}_\alpha \\ \hat{i}_\beta \end{bmatrix} \\ \qquad\qquad + \dfrac{1}{L_s}\begin{bmatrix} u_\alpha \\ u_\beta \end{bmatrix} - \dfrac{1}{L_s}\begin{bmatrix} v_\alpha \\ v_\beta \end{bmatrix} \\ \begin{bmatrix} v_\alpha \\ v_\beta \end{bmatrix} = \begin{bmatrix} k_s \operatorname{sgn}\left(\hat{i}_\alpha - i_\alpha\right) \\ k_s \operatorname{sgn}\left(\hat{i}_\alpha - i_\alpha\right) \end{bmatrix}. \end{cases} \quad \text{(C2)}$$

where $\hat{i}_\alpha$ and $\hat{i}_\beta$ are the observed values of stator current, k_s is the sliding mode gain and its value is designed by Lyapunov theory. Then (C2) subtract (C1) becomes:

$$\frac{\mathrm{d}}{\mathrm{d}t}\begin{bmatrix} \hat{i}_\alpha - i_\alpha \\ \hat{i}_\beta - i_\beta \end{bmatrix} = \frac{1}{L_s}\begin{bmatrix} -R_s & 0 \\ 0 & -R_s \end{bmatrix}\begin{bmatrix} \hat{i}_\alpha - i_\alpha \\ \hat{i}_\beta - i_\beta \end{bmatrix} + \frac{1}{L_s}\begin{bmatrix} E_\alpha - v_\alpha \\ E_\beta - v_\beta \end{bmatrix}. \quad \text{(C3)}$$

In order to estimate E_α and E_β, the sliding mode surface is defined as $\boldsymbol{s} = \begin{bmatrix} \hat{i}_\alpha - i_\alpha & \hat{i}_\beta - i_\beta \end{bmatrix}^T$. When the state variables of SMO reach the sliding mode surface, the back EMF can be expressed as follows:

$$\begin{bmatrix} E_\alpha \\ E_\beta \end{bmatrix} = \begin{bmatrix} v_\alpha \\ v_\beta \end{bmatrix} = \begin{bmatrix} k_s \operatorname{sgn}\left(\hat{i}_\alpha - i_\alpha\right) \\ k_s \operatorname{sgn}\left(\hat{i}_\alpha - i_\alpha\right) \end{bmatrix}. \quad \text{(C4)}$$

The rotor position can be extracted from the estimated back EMF. A simple method is to use an arctangent function, while it sensitive to system noise. In this paper, the PLL is used to extract the position information, as shown in Fig. 34.

Besides, the estimated position error is normalized to improve the stability of PLL. Due to the back EMF related to the rotor speed, the poles of the transfer function of PLL-based estimator may vary with different speeds, which will transform the response performance of PLL. The normalized position error is expressed as

$$\delta_E = \frac{1}{\sqrt{E_\alpha^2 + E_\beta^2}}\left[-E_\alpha \cos\left(\theta_e\right) - E_\beta \sin\left(\hat{\theta}_e\right)\right]. \quad \text{(C5)}$$

The estimated position can be obtained as follows:

$$\hat{\theta}_e = (1/s)\left(k_p + k_i/s\right)\delta_E \quad \text{(C6)}$$

where k_p and k_i are the proportion and integration coefficients of PI controller, respectively.

APPENDIX D. BASIC PRINCIPLE OF DPCC

According to Euler's method, the dq-axis voltage equations of PMSM can be discretized as follows: [38]

$$\begin{cases} u_d(k) = R_s i_d(k) + (L_d/T)\left[i_d(k+1) - i_d(k)\right] \\ \qquad\qquad -\omega_e L_q i_q(k) \\ u_q(k) = R_s i_q(k) + (L_q/T)\left[i_q(k+1) - i_q(k)\right] \\ \qquad\qquad +\omega_e L_d i_d(k) + \omega_e \psi_m \end{cases} \quad \text{(D1)}$$

where u_d and u_q are actual dq-axis voltages.

In (D1), replacing $i_d(k+1)$ and $i_q(k+1)$ with the reference currents $i_d^*(k)$ and $i_q^*(k)$, the predicted voltages $u_d^{pre}(k)$ and $u_q^{pre}(k)$ can be obtained as follows:

$$\begin{cases} u_d^{pre}(k) = R_s i_d(k) + (L_d/T)\left[i_d^*(k) - i_d(k)\right] \\ \qquad\qquad -\omega_e L_q i_q(k) \\ u_q^{pre}(k) = R_s i_q(k) + \left(L_q/T\right)\left[i_q^*(k) - i_q(k)\right] \\ \qquad\qquad +\omega_e L_d i_d(k) + \omega_e \psi_m. \end{cases} \quad \text{(D2)}$$

In a microprocessor, $i_d(k+1)$ and $i_q(k+1)$ are generated by the previous predicted voltages [38]. Thus, it is necessary to predict $i_d(k+1)$ and $i_q(k+1)$ to improve the accuracy of voltage prediction, as shown below:

$$\begin{cases} i_d^{\text{com}}(k+1) = (1 - R_s T/L_s) i_d(k) + T\omega_e i_q(k) \\ \qquad\qquad +u_d^{pre}(k-1)T/L_s \\ i_q^{\text{com}}(k+1) = (1 - R_s T/L_s) i_q(k) - T\omega_e i_d(k) \\ \qquad\qquad +u_q^{pre}(k-1)T/L_s - \omega_e \psi_m T/L_s \end{cases} \quad \text{(D3)}$$

where the superscript $^{\text{com}}$ represents the delay compensation.

Finally, substituting (D3) into (D2) yields:

$$\begin{cases} u_d^{pre}(k) = R_s i_d^{com}(k+1) + (L_d/T)\left[i_d^*(k) - i_d^{com}(k+1)\right] \\ \qquad\qquad -\omega_e L_q i_q(k) \\ u_q^{pre}(k) = R_s i_q^{com}(k+1) + \left(L_q/T\right)\left[i_q^*(k) - i_q^{com}(k+1)\right] \\ \qquad\qquad +\omega_e L_d i_d^{com}(k+1) + \omega_e \psi_m. \end{cases} \quad \text{(D4)}$$

Equations (D3) and (D4) are the core models of DPCC, and their specific applications are shown in Fig. 16(b).

REFERENCES

[1] G. Liu, B. Chen, K. Wang, and X. Song, "Selective current harmonic suppression for high-speed PMSM based on high-precision harmonic detection method," *IEEE Trans. Ind. Informat.*, vol. 15, no. 6, pp. 3457–3468, Jun. 2019.

[2] K. Liu and Z. Zhu, "Fast determination of moment of inertia of permanent magnet synchronous machine drives for design of speed loop regulator," *IEEE Trans. Control Syst. Technol.*, vol. 25, no. 5, pp. 1816–1824, Sep. 2017.

[3] S. M. Seyyedzadeh and A. Shoulaie, "Accurate modeling of the nonlinear characteristic of a voltage source inverter for better performance in near zero currents," *IEEE Trans. Ind. Electron.*, vol. 66, no. 1, pp. 71–78, Jan. 2019.

[4] G. Wang, H. Zhan, G. Zhang, X. Gui, and D. Xu, "Adaptive compensation method of position estimation harmonic error for EMF-based observer in sensorless IPMSM drives," *IEEE Trans. Power Electron.*, vol. 29, no. 6, pp. 3055–3064, Jun. 2014.

[5] X. Zhang, B. Hou, and Y. Mei, "Deadbeat predictive current control of permanent-magnet synchronous motors with stator current and disturbance observer," *IEEE Trans. Power Electron.*, vol. 32, no. 5, pp. 3818–3834, May 2017.

[6] D. Leggate and R. J. Kerkman, "Pulse-based dead-time compensator for PWM voltage inverters," *IEEE Trans. Ind. Electron.*, vol. 44, no. 2, pp. 191–197, Apr. 1997.

[7] P. J. Patel, V. Patel, and P. N. Tekwani, "Pulse-based dead-time compensation method for self-balancing space vector pulse width-modulated scheme used in a three-level inverter-fed induction motor drive," *IET Power Electron.*, vol. 4, no. 6, pp. 624–631, Jul. 2011.

[8] K. D. Hoang and H. K. A. Aorith, "Online control of IPMSM drives for traction applications considering machine parameter and inverter nonlinearities," *IEEE Trans. Transport. Electrific.*, vol. 1, no. 4, pp. 312–325, Dec. 2015.

[9] Q. Yan, P. Sun, L. Xiao, R. Zhao, and H. Xu, "A combined DPWM based on DSOGI-FLL for switching-loss reduction and dead-time compensation," *IEEE Access*, vol. 8, pp. 34783–34793, 2020.

[10] W. Dafang, Y. Bowen, Z. Cheng, Z. Chuanwei, and Q. Ji, "A feedback-type phase voltage compensation strategy based on phase current reconstruction for ACIM drives," *IEEE Trans. Power Electron.*, vol. 29, no. 9, pp. 5031–5043, Sep. 2014.

[11] D. H. Lee and J. W. Ahn, "A simple and direct dead-time effect compensation scheme in PWM-VSI," *IEEE Trans. Ind. Appl.*, vol. 50, no. 5, pp. 3017–3025, Oct. 2014.

[12] Z. Shen and D. Jiang, "Dead-time effect compensation method based on current ripple prediction for voltage-source inverters," *IEEE Trans. Power Electron.*, vol. 34, no. 1, pp. 971–983, Jan. 2019.

[13] G. Liu, D. Wang, Y. Jin, M. Wang, and P. Zhang, "Current-detection-independent dead-time compensation method based on terminal voltage A/D conversion for PWM VSI," *IEEE Trans. Ind. Electron.*, vol. 64, no. 10, pp. 7689–7699, Oct. 2017.

[14] Y. K. Lin and Y. S. Lai, "Dead-time elimination of PWM-controlled inverter/converter without separate power sources for current polarity detection circuit," *IEEE Trans. Ind. Electron.*, vol. 56, no. 6, pp. 2121–2127, Jun. 2009.

[15] X. Wang, S. Nalakath, S. Filho, G. Zhao, Y. Sun, J. Wiseman, and A. Emadi, "A simple and effective compensation method for inverter nonlinearity," in *Proc. IEEE Transp. Electrific. Conf. Expo (ITEC)*, Chicago, IL, USA, Jun. 2020, pp. 638–643.

[16] D. Liang, J. Li, R. Qu, and W. Kong, "Adaptive second-order sliding-mode observer for PMSM sensorless control considering VSI nonlinearity," *IEEE Trans. Power Electron.*, vol. 33, no. 10, pp. 8994–9004, Oct. 2018.

[17] D.-M. Park and K.-H. Kim, "Parameter-independent online compensation scheme for dead time and inverter nonlinearity in IPMSM drive through waveform analysis," *IEEE Trans. Ind. Electron.*, vol. 61, no. 2, pp. 701–707, Feb. 2014.

[18] G. Pellegrino, P. Guglielmi, E. Armando, and R. I. Bojoi, "Self-commissioning algorithm for inverter nonlinearity compensation in sensorless induction motor drives," *IEEE Trans. Ind. Appl.*, vol. 46, no. 4, pp. 1416–1424, Jul. 2010.

[19] Y. Wang, Y. Xu, and J. Zou, "ILC-based voltage compensation method for PMSM sensorless control considering inverter nonlinearity and sampling current DC bias," *IEEE Trans. Ind. Electron.*, vol. 67, no. 7, pp. 5980–5989, Jul. 2020.
[20] Y. Wang, Y. Xu, and J. Zou, "Sliding-mode sensorless control of PMSM with inverter nonlinearity compensation," *IEEE Trans. Power Electron.*, vol. 34, no. 10, pp. 10206–10220, Oct. 2019.
[21] G. Feng, C. Lai, K. Mukherjee, and N. C. Kar, "Current injection-based online parameter and VSI nonlinearity estimation for PMSM drives using current and voltage DC components," *IEEE Trans. Transport. Electrific.*, vol. 2, no. 2, pp. 119–128, Jun. 2016.
[22] K. Liu and Z. Q. Zhu, "Online estimation of the rotor flux linkage and voltage-source inverter nonlinearity in permanent magnet synchronous machine drives," *IEEE Trans. Power Electron.*, vol. 29, no. 1, pp. 418–427, Jan. 2014.
[23] T. Liu, Q. Li, Q. Tong, Q. Zhang, and K. Liu, "An adaptive strategy to compensate nonlinear effects of voltage source inverters based on artificial neural networks," *IEEE Access*, vol. 8, pp. 129992–130002, 2020.
[24] Q. Yuan, Y. Yang, H. Wu, and H. Wu, "Low speed sensorless control based on an improved sliding mode observation and the inverter nonlinearity compensation for SPMSM," *IEEE Access*, vol. 8, pp. 61299–61310, 2020.
[25] H.-S. Kim, H.-T. Moon, and M.-J. Youn, "On-line dead-time compensation method using disturbance observer," *IEEE Trans. Power Electron.*, vol. 18, no. 6, pp. 1336–1345, Nov. 2003.
[26] H. W. Kim, H. S. Kim, M. J. Youn, and K. W. Cho, "Online observation and compensation of voltage distortion in PWM VSI for PMSM," *IEE Proc. Elect. Power Appl.*, vol. 151, no. 5, pp. 534–542, Sep. 2004.
[27] H.-S. Kim, K.-H. Kim, and M.-J. Youn, "On-line dead-time compensation method based on time delay control," *IEEE Trans. Control Syst. Technol.*, vol. 11, no. 2, pp. 279–285, Mar. 2003.
[28] H.-W. Kim, M.-J. Youn, K.-Y. Cho, and H.-S. Kim, "Nonlinearity estimation and compensation of PWM VSI for PMSM under resistance and flux linkage uncertainty," *IEEE Trans. Control Syst. Technol.*, vol. 14, no. 4, pp. 589–601, Jul. 2006.
[29] N. Urasaki, T. Senjyu, K. Uezato, and T. Funabashi, "Adaptive dead-time compensation strategy for permanent magnet synchronous motor drive," *IEEE Trans. Energy Convers.*, vol. 22, no. 4, pp. 271–280, Jun. 2007.
[30] S. Zhu, W. Huang, and Y. Yan, "A simple inverter nonlinearity compensation method using on-line voltage error observer," in *Proc. 22nd Int. Conf. Electr. Mach. Syst. (ICEMS)*, Harbin, China, Aug. 2019, pp. 1–6.
[31] H. Ge, Y. Miao, B. Bilgin, B. Nahid-Mobarakeh, and A. Emadi, "Speed range extended maximum torque per ampere control for PM drives considering inverter and motor nonlinearities," *IEEE Trans. Power Electron.*, vol. 32, no. 9, pp. 7151–7159, Sep. 2017.
[32] C. Lai, G. Feng, K. Mukherjee, J. Tjong, and N. C. Kar, "Maximum torque per ampere control for IPMSM using gradient descent algorithm based on measured speed harmonics," *IEEE Trans. Ind. Informat.*, vol. 14, no. 4, pp. 1424–1435, Apr. 2018.
[33] Z. Zhou, C. Xia, Y. Yan, Z. Wang, and T. Shi, "Disturbances attenuation of permanent magnet synchronous motor drives using cascaded predictive-integral-resonant controllers," *IEEE Trans. Power Electron.*, vol. 33, no. 2, pp. 1514–1527, Feb. 2018.
[34] G. Feng, C. Lai, and N. C. Kar, "Speed harmonic based modeling and estimation of permanent magnet temperature for PMSM drive using Kalman filter," *IEEE Trans. Ind. Informat.*, vol. 15, no. 3, pp. 1372–1382, Mar. 2019.
[35] N. Pothi, "Improvement of flux-weakening control of surface mounted permanent magnet synchronous machine considering inverter nonlinearity," in *Proc. Int. Electr. Eng. Congr. (iEECON)*, Pattaya, Thailand, Mar. 2017, pp. 1–4.
[36] H. Lee and J. Lee, "Design of iterative sliding mode observer for sensorless PMSM control," *IEEE Trans. Control Syst. Technol.*, vol. 21, no. 4, pp. 1394–1399, Jul. 2013.
[37] W. Xu, L. Wang, Y. Liu, and F. Blaabjerg, "Improved rotor flux observer for sensorless control of PMSM with adaptive harmonic elimination and phase compensation," *CES Trans. Electr. Mach. Syst.*, vol. 3, no. 2, pp. 151–159, Jun. 2019.
[38] Z. Wang, A. Yu, X. Li, G. Zhang, and C. Xia, "A novel current predictive control based on fuzzy algorithm for PMSM," *IEEE J. Emerg. Sel. Topics Power Electron.*, vol. 7, no. 2, pp. 990–1001, Jun. 2019.

SHICHAO ZHOU received the B.Eng. degree in vehicle engineering from Hunan University, Changsha, China, in 2019, where he is currently pursuing the Ph.D. degree in mechanical and vehicle engineering. His main current research interests include the suppression of harmonic and circulating-current in the permanent magnet synchronous machine drive systems.

KAN LIU (Senior Member, IEEE) received the B.Eng. and Ph.D. degrees in automation from Hunan University, Changsha, China, in 2005 and 2011, respectively, and the Ph.D. degree in electronic and electrical engineering from The University of Sheffield, Sheffield, U.K., in 2013.

From 2013 to 2016, he was a Research Associate with the Department of Electronic and Electrical Engineering, The University of Sheffield. From 2016 to 2017, he was a Lecturer with the Control Systems Group, Loughborough University. He is currently a Professor of electromechanical engineering with Hunan University. He is also the Director with the Engineering Research Center of Ministry of Education on Automotive Electronics and Control Technology, China. His research interests include parameters estimation and sensorless control of permanent magnet synchronous machine drives, advanced design, and control solutions of high-power density converters, for applications ranging from electric locomotive and automotive, to servo motor, and drive. He serves as an Associate Editor for IEEE Access and the *CES Transactions on Electrical Machines and Systems*.

WEI HU received the B.Eng. and M.Sc. degrees in electrical engineering from Harbin Institute of Technology, Harbin, China, in 2014 and 2016, respectively, and the Ph.D. degree in electrical engineering from Zhejiang University, Hangzhou, China, in 2020.

He is currently an Assistant Professor with Hunan University. His main current research interests include the structure and drives of open-winding permanent magnet synchronous motors.

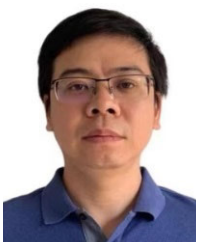

YONGDAN CHEN received the Ph.D. degree in mechatronics engineering from Beijing Institution of Technology, Beijing, China, in 2012. In 2012, he joined the State Key Laboratory of Vehicle Transmission, China North Vehicle Research Institute, where he has been a Professor of vehicle engineering and a Leader of Electric Drive Group, since 2018. His current major research interests include the application, control, and design of electric dive.

DINGHUA ZHANG received the B.Eng. degree in automation from Hunan University of Science and Technology, Xiangtan, China, in 2003, and the M.Eng. and Ph.D. degrees from Central South University, Changsha, China, in 2006 and 2011, respectively.

He is currently a Professor-Level Senior Engineer and a Senior Technical Expert at CRRC. He is now engaged in technical development and management of subsea equipment. And he is the Deputy General Manager and a Chief Engineer at Shanghai SMD Company Ltd. His research interests include the remote operated vehicle control and power conversion control.

QING HUANG received the Ph.D. degree in electrical engineering from Hunan University, Changsha, China, in 2014. He is currently a Senior Engineer with China Railway Rolling Stock Corporation and the Deputy General Manager with Hunan Lixing Power Technology Company Ltd. His main research interests include electric drive systems, power supply technology, and fault diagnosis/prediction.

QIAOLING TONG (Member, IEEE) received the B.Eng. and Ph.D. degrees from the School of Optical and Electronic Information, Huazhong University of Science and Technology, China, in 2003 and 2010, respectively. From 2008 to 2010, he was a Research Scholar with the Department of Electrical Engineering and Computer Science, University of California at Irvine, Irvine. He is currently an Associate Professor with the School of Optical and Electronic Information, Huazhong University of Science and Technology. His current research interests include sensorless control of dc–dc converters and VLSI implementation of intelligent algorithms.

QIAO ZHANG (Member, IEEE) received the B.Eng., M.Eng., and Ph.D. degrees from the Huazhong University of Science and Technology, Wuhan, China, in 2003, 2006, and 2010, respectively. From 2008 to 2009, he was a Visiting Scholar with the Department of Electronic and Electrical Engineering, The University of Sheffield, U.K. From 2009 to 2016, he was a Research Engineer with IMRA Europe U.K. Research Centre. He is currently an Associate Professor with the School of Automation, Wuhan University of Technology. His research interests include the power electronics system design and control, such as dc–dc converter sensorless control strategies, electrical machine parameters estimation by control theory, system nonlinearity compensation for dc–dc converters, and voltage source inverters.